Structure and function of an intermediate GPCR-Gαβγ complex

Maxine Bi[1#], Xudong Wang[2#], Jinan Wang[3#], Jun Xu[4], Wenkai Sun[2], Victor Ayo Adediwura[3], Yinglong Miao[3*], Yifan Cheng[1,5*], Libin Ye[2,6*]

[1]Department of Biochemistry and Biophysics, University of California, San Francisco, CA 94143
[2]Department of Molecular Biosciences, University of South Florida, 4202 E Fowler Ave, Tampa, FL USA 33620
[3]Department of Pharmacology & Computational Medicinal Program, University of North Carolina at Chapel Hill, 116 Manning Drive, 11004C Mary Ellen Jones Building, Chapel Hill, NC 27599
[4]Department of Molecular and Cellular Physiology, Stanford University School of Medicine, Stanford, CA, USA
[5]Howard Hughes Medical Institute, University of California, San Francisco, CA 94143
[6]H. Lee Moffitt Cancer Center & Research Institute, 12902 USF Magnolia Drive, Tampa, FL, USA 33612

***Corresponding author**

Yinglong Miao, Associate Professor

Department of Pharmacology & Computational Medicinal Program, 116 Manning Drive, 11004C Mary Ellen Jones Building, Chapel Hill, NC 27599
E-mail: Yinglong_Miao@med.unc.edu Tel: 1-919-962-5696

Yifan Cheng, Professor

Department of Biochemistry and Biophysics, University of California, San Francisco, CA 94143; Howard Hughes Medical Institute, University of California, San Francisco, CA 94143

E-mail: Yifan.Cheng@ucsf.edu Tel: 1-415-514-9707

Libin Ye, Assistant Professor

Department of Molecular Biosciences, University of South Florida, 4202 E Fowler Ave, Tampa, FL, USA 33620; H. Lee Moffitt Cancer Center & Research Institute, 12902 USF Magnolia Drive, Tampa, FL, USA 33612

E-mail: libinye@usf.edu Tel: 1-813-974-6007

Abstract

Unraveling the signaling roles of intermediate complexes is pivotal for G protein-coupled receptor (GPCR) drug development. Despite hundreds of GPCR-Gαβγ structures, these snapshots primarily capture the fully activated end-state complex. Consequently, a comprehensive understanding of the conformational transitions during GPCR activation and the roles of intermediate GPCR-G protein complexes in signaling remain elusive. Guided by a conformational landscape profiled by ^{19}F quantitative NMR (^{19}F-qNMR) and Molecular Dynamics (MD) simulations, we resolved the structure of an unliganded GPCR-G protein intermediate complex by blocking its transition to the fully activated end-state complex. More importantly, we presented direct evidence that the intermediate GPCR-$G\alpha_s\beta\gamma$ complex initiates a rate-limited nucleotide exchange without progressing to the fully activated end-state complex, thereby bridging a significant gap in our understanding the complexity of GPCR signaling. Understanding the roles of individual conformational states and their complexes in signaling efficacy and bias will help us to design drugs that discriminately target a disease-related conformation.

68 **Main**

69 G protein-coupled receptors (GPCRs) are the largest family of human membrane proteins,
70 encompassing over 800 distinct members. Due to their vital roles in various
71 (patho)physiological processes, significant efforts have been made to unravel their
72 activation mechanisms, aiming to modulate therapeutic signaling with precision. Recent
73 advancements, especially in single-particle cryo-electron microscopy (cryo-EM), have
74 facilitated the structural determination of hundreds of GPCR-G$\alpha\beta\gamma$ complex since 2017[1-
75 3]. These complex structures primarily represent the receptors in their fully activated end-
76 states. Yet, the GPCR signaling process is more intricate than what these structures
77 alone can depict. Multiple studies have shown that GPCR activation entails transitions
78 through several intermediate complexes, including pre-coupled and partially activated
79 GPCR-G protein complexes[4-12]. Isolating such transient complexes to study their
80 signaling roles presents a significant challenge.

81

82 Using the adenosine-A_{2A} receptor ($A_{2A}R$) as a model system and applying ^{19}F quantitative
83 NMR (^{19}F-qNMR), we mapped the conformational landscape of this GPCR in response
84 to ligand actions. Within this landscape, we identified two transient active-like
85 intermediates (S3 and S4) that are positioned between the inactive (defined as S1 and
86 S2) and the fully activated states (S5)[13] (Fig. 1a). Among these conformations, S1 and
87 S2 have been defined by crystal structures [14,15], and the S5 state has been characterized
88 by cryo-EM (PDB ID: 6GDG)[16] (Fig. 1b and Extended Data Fig. 1). The structures of S3
89 and S4, however, remain uncharacterized. With the R291A point mutation, which we
90 previously determined to trap $A_{2A}R$ uniquely in the intermediate S4 state (Fig. 1)[13], we
91 have continued to investigate the structure and function of this intermediate state. Our
92 study seeks to answer questions such as whether the intermediate S4 can directly interact
93 with and regulate G protein without transitioning to the S5 state and how the G protein
94 responds to the intermediate S4. Understanding the structural and functional roles of
95 individual intermediate GPCR-G protein complexes will significantly advance our
96 knowledge at the molecular mechanistic level regarding the signaling efficacy, bias, and
97 allostery, which is pivotal for improving drug designs[5,17,18].

98

S4 state binds to $G\alpha_s\beta\gamma$ and initiates nucleotide exchange

We first examined whether the WT*-R291A mutant, which is trapped in the S4 state, can bind to the $G\alpha\beta\gamma$. Here, the S4 trapped mutant was introduced to a previously defined construct ($A_{2A}R$-316-V229C, denoted as WT*),[13] and we referred to WT*-R291A simply as R291A. We incubated ^{19}F-labeled R291A with $G\alpha\beta\gamma$, subjected it to ^{19}F-NMR, and measured the linewidth of the NMR resonance. Indeed, we observed a linewidth broadening for the S4 resonance compared to the receptor alone, suggesting direct binding of $G\alpha\beta\gamma$ to $A_{2A}R$ in the S4 state (Extended Data Fig. 2a). This was further confirmed by a complex band of apo R291A-$G\alpha_s\beta\gamma$ in native-PAGE (Extended Data Fig. 2b).

Next, we assessed how the S4 regulates G protein function by performing nucleotide hydrolysis, binding, and exchange assays. As shown in Fig. 2a, the R291A mutant-mediated GTP hydrolysis from the G protein occurred at a much slower rate compared to the full agonist-bound WT*-$G\alpha_s\beta\gamma$ (representing the S5-$G\alpha_s\beta\gamma$). However, the addition of full, partial, or inverse agonists did not alter the GTP hydrolysis level substantially in the R291A mutant. This ligand-independent hydrolysis behavior is in stark contrast to the wild-type construct, where ligand binding dramatically changes the hydrolysis level[19,20]. To further investigate the reduced hydrolysis level, we measured the initial rates and Michaelis constants of GTP hydrolysis. The initial rate of GTP hydrolysis mediated by R291A was only one-twentieth of that mediated by WT* (Fig. 2b), while the Michaelis constant exhibited a similar pattern (Fig. 2c).

We proposed a simple model to explain the limited GTP hydrolyzing capacity of the S4-mediated G protein, where nucleotide binding to G protein is a two-step process. A nucleotide GTP initially binds to a site with low affinity and hydrolysis (site1) in the intermediate S4-G protein complex. Upon the transitioning from S4 to S5, the G protein changes its conformation to allow the GTP to access the site 2, the canonical nucleotide-binding site. We tested this model by examining the binding of BODIPY-FL-GDP (Figs. 2d and 2h). The BODIPY-FL-GDP bound to the WT*-mediated G protein exhibited a higher K_D than that of the R291A-mediated G protein, although both reached equilibrium

130 at 1.5 hrs. For the R291A-mediated G protein, a secondary association event was
131 observed after 1.5 hrs with a K_D value 10 times lower, which was not the case observed
132 in the WT*. We attribute this difference to the restricted accessibility of the site 2, caused
133 by spatial constraints resulting from the partially open AHD domain in the S4 mediated
134 G-protein, while this site is freely accessible in the WT*. A similar pattern was noted in
135 BODIPY-FL-GTP binding assays, where BODIPY-FL-GTP showed more efficient binding
136 to the S5-mediated G protein with a higher K_D value (Fig. 2e and 2h). The spatial limited
137 association process was also evident in BODIPY-FL-GTP-γ-S (Fig.2f) in both S5 and S4
138 mediated G protein because the BODIPY head was linked to γ-phosphate, which is meant
139 to be inserted into the site 2. The bulky BODIPY head insertion restricted exchange and
140 hydrolysis. Titration of GTP into the BODIPY-FL-GDP equilibrium system led us to
141 conclude that the S4-mediated G protein has a reduced nucleotide exchange rate
142 compared to the S5-mediated G protein (Fig. 2g). A previous study of β_2AR indicated that
143 GDP release occurs much faster than the formation of fully activated complex[21], while
144 MD simulations suggested that GDP is released when the $G\alpha_s$ is not fully opened[22].
145 Collectively, our data suggests the intermediate S4 state mediated G-protein initiates
146 nucleotide exchange before transitioning to the fully activated S5 state, albeit at a reduced
147 rate.
148
149 **Structure of the ligand-free intermediate S4-mini-$G\alpha_s\beta\gamma$ complex**
150 Building upon the two-step nucleotide binding model, we hypothesized that the S4 state
151 not only adopts a conformation distinct from S5 but also binds to the G protein in a manner
152 conformationally different from the S5-bound state. To test this hypothesis and enhance
153 our understanding of the molecular mechanisms involved, we aimed to determine the
154 structure of the intermediate S4 state in complex with the G protein.
155
156 To capture the structure of intermediate S4 state in complex with G proteins, we
157 assembled a stable complex by incubating the R291A mutation with mini-$G\alpha_s$, known as
158 mini-$G\alpha_s$399, and the $G\alpha_s$-stabilizing nanobody, NB35, in conjunction with Gβ1γ2. As
159 evidenced by ^{19}F-qNMR, the receptor preserves the conformation of the S4 state in
160 complex with G proteins (Fig.1b and 1c). We determined a cryo-EM structure of this S4-

161 mini-G$\alpha_s\beta\gamma$ complex at a 2.8 Å resolution, revealing the key interaction sites between
162 $A_{2A}R$ and mini-G$\alpha_s\beta\gamma$ without ligand (Figs. 1d-f and Fig.3a). For a comprehensive
163 understanding of our methods, we have detailed the sample preparation, cryo-EM data
164 acquisition, and processing steps in Extended Data Figs. 3-6, and Supplementary Table
165 1.
166
167 Comparisons of the S4-mini-G$\alpha_s\beta\gamma$ complex with the S5-mini-G$\alpha_s\beta\gamma$ complex (PDB ID:
168 6GDG), as depicted in Supplementary videos 1 and 2, reveal key differences between
169 the two states. The extracellular orthosteric binding pocket of the intermediate complex
170 S4-mini-G$\alpha_s\beta\gamma$ is less compact than of the S5-mini-G$\alpha_s\beta\gamma$ (Fig. 3b), yet more constricted
171 compared to the inactive state[14,15]. Transitioning from the inactive to the intermediate
172 state S4 involves significant inward movements of all domains relative to TM1 in the
173 extracellular domains. The shift from the intermediate to the fully activated complex
174 results in observable movements of these domains. This is consistent with the ^{19}F-qNMR
175 study, which recorded a substantial chemical shift (~400 Hz) when the receptor
176 transitioned from the inactive states S1-2 to intermediate S4, while the shift from S4 to S5
177 resulted in a minor chemical shift (~60 Hz) (Fig.3f). Closer inspection of the TM6 domain,
178 using the ^{19}F-tag labeling site as a reference, revealed a clockwise rotation consistent
179 with the ^{19}F-qNMR resonance, where the NMR signal for the S4 state is at a lower field
180 than the S5 state. Indeed, the conformation of the intermediate S4 state is thus on the
181 trajectory from the inactive S1-2 to the fully activated S5 states.
182
183 One of the key microswitches in the receptor is the $\underline{P^{5.50}I^{3.40}F^{6.44}}$ motif, which is a crucial
184 hydrophobic switch between TM5, TM3 and TM6 and is implicated in receptor
185 activation[1,23]. In the fully activated receptor, $P^{5.50}$ and $F^{6.44}$ are in cis positions, forming a
186 strong CH-π interaction[24], and the CH_3 group of $I^{3.40}$ also forms a robust CH_3-π interaction
187 with $F^{6.44}$, stabilizing the fully activated conformation. In contrast, these interactions are
188 weakened in the S4-mini-G$\alpha_s\beta\gamma$ complex because $P^{5.50}$ and $I^{3.40}$ are oriented away from
189 $F^{6.44}$ (Fig. 3d). Another key microswitch is the $\underline{CW^{6.48}xP}$ motif, where $P^{6.50}$ acts as a hinge
190 in TM6 and facilitates the opening of the cytoplasmic cavity during activation[25]. Our cryo-
191 EM structure clearly shows $P^{6.50}$ in an "intermediate" position, bridging the inactive and

192 active states (Fig. 3e). The third microswitch, the NPxxY$^{7.53}$ on TM7, along with a
193 conserved tyrosine Y$^{5.58}$ in TM5, stabilizes the receptor's active state[26-28]. As illustrated in
194 Fig. 3g, a strong H-bond is observed between Y$^{5.58}$ and Y$^{7.53}$ in the S5-mini-G$\alpha\beta\gamma$ complex.
195 This interaction draws Y$^{5.58}$ on TM5 closer to TM7, maintaining the compactness of the
196 TM bundle in the S5-G protein complex, as shown in the animation from the S4-mini-
197 G$\alpha_s\beta\gamma$ transitioning to the S5-mini-G$\alpha\beta\gamma$ (Supplementary videos 1 and 2). Therefore,
198 transitioning from the S4- to the S5-mini-G$\alpha_s\beta\gamma$ strengthens the H-bond interaction as
199 Y$^{5.58}$ moves closer to the TM7 domain, aiding in the insertion of the G protein into the
200 cavity. Our analysis indeed supports the idea that the S4 conformation can regulate G
201 protein signaling to some degree without transitioning to the fully activated S5 state.
202
203 Next, we examined the interfacial interaction between Cα5 helix of mini-Gα_s (Fig. 3c) and
204 the transmembrane bundle comprising TM3, TM6 and TM7 domains - critical components
205 in regulating G protein nucleotide exchange. As highlighted in Fig. 3c, the S4-mini-G$\alpha_s\beta\gamma$
206 adopts a slightly more open conformation than the S5-mini-G$\alpha_s\beta\gamma$. The Cα5 helix is
207 significantly rotated outward and retracted from the G protein-binding pocket,
208 accompanied by the disengagement of the αN helix of the Gα_s protein from the H8 helix
209 of the receptor. This retraction measures approximately 2 Å and the rotation is at a 2°
210 spinal clockwise angle from the S5-mini-G$\alpha_s\beta\gamma$. This motion is further detailed in Fig. 3h,
211 which shows the primary interactions at the junction composed of TM3, TM6, TM7
212 domains, and the Cα5 segment from mini-Gα_s. During the activation process, the
213 clockwise rotation of TM6 and counterclockwise rotation of Cα5 culminate in a compact
214 end-state complex. The transition from the S4- to the S5-mini-G$\alpha_s\beta\gamma$ entails a further
215 insertion of the G protein and an inward rotation of the receptor domain, evidenced by the
216 formation of the salt bridge R$^{7.56}$-E392$^{G\alpha}$ and the cation-π interaction between R$^{7.56}$ and
217 H$^{6.32}$, coupled with a strengthened cation-π interaction between R$^{3.50}$ and Y391$^{G\alpha}$.
218 However, the R$^{7.56}$ to A$^{7.56}$ mutation eliminates this interaction.
219
220 **Molecular basis of A_{2A}R function in the S4 state**

221 To validate the conformational transition between the S4 and S5 states, we applied all-
222 atom Gaussian accelerated MD (GaMD) simulations, starting from atomic structure of the
223 S5-mini-G$\alpha_s\beta\gamma$ complex (6GDG) with a R291A mutation modeled in silico. Indeed, the
224 R291A mutation facilitated transition of the 6GDG structure (S5 state, Fig.1b) to an energy
225 minimum conformation that closely matches our new cryo-EM structure. We refer to this
226 as cS4 state, where "c" stands for computational model, and here the Cα5 helix in Gα_s
227 retracted from the receptor by ~2 Å. The center-of-mass distance between the receptor
228 NPxxY motif and the last five residues of Cα5 helix increased from ~13.2 Å in the "S5"
229 state to ~15.3 Å in the "cS4" state (Fig. 4a and Extended Data Fig. 7). As a control, GaMD
230 simulations showed that the cWT-mini-G$\alpha_s\beta\gamma$ complex remained stable, mainly sampling
231 one low-energy state, corresponding to the S5 (Fig.4b). These simulations independently
232 validated the conformation of the intermediate S4 state determined from single particle
233 cryo-EM.
234
235 Furthermore, we performed additional GaMD simulations to examine GDP release. In the
236 cWT-G$\alpha_s\beta\gamma$ system, GDP was observed moving away from the initial binding site by up
237 to ~12 Å repeatedly (Fig.4c). In contrast, GDP underwent significantly smaller movements
238 up to only ~8 Å in the cR291A-G$\alpha_s\beta\gamma$ system (Fig. 4f). Free energy calculations also
239 indicated a "GDP Released" state in the cWT-G$\alpha_s\beta\gamma$ system and only a "Partially
240 Released" state in the cR291A-G$\alpha_s\beta\gamma$ system (Extended Data Figs. 8a-c), where the AHD
241 domain of Gα_s transitioned from the "Open" to "Partially Open" conformation, with the
242 orientation angle between the AHD and Ras-like domain decreasing to ~30° (Extended
243 Data Figs. 8d-e) [1,29]. Together, these observations suggest that the S4 state mediated G
244 protein has a reduced capacity for GDP release compared to the S5 state, aligning with
245 the nucleotide exchange data shown above.
246
247 **A limited nucleotide exchange model for intermediate GPCR-G$\alpha_s\beta\gamma$ complex**
248 A mechanistic model is proposed to understand the rate-limited nucleotide exchange in
249 the intermediate GPCR-G protein complex (Fig.5). The transition from the intermediate
250 to the fully activated complex involves a conformational change at the interface, where
251 the TM6 helix of the receptor rotates clockwise by 8° while the Cα5 helix from the Ras-

like domain rotates anticlockwise by 2°. This leads to a more compact interaction between the receptor and G protein, coupled with a 2 Å uplift of the Cα5 helix. This uplift results in the disengagement of the H1 from the Cα5 helix, facilitating the separation of AHD domain from Ras-like domain and thereby exposing the bound GDP at site 2. Simultaneously, this process assists the relocation of GTP from site 1 to site 2, replacing GDP. However, in the S4-mediated G protein, the substitution of $R^{7.56}$ with alanine ($A^{7.56}$) results in the loss of both the intramolecular cation-π ($R^{7.56}$-$H^{6.32}$) interaction and the intermolecular salt bridge ($R^{7.56}$-$E392^{G\alpha}$). Instead, a partially opened AHD domain is seen (Fig.4e), which can be attributed to a weak electrostatic H-bond (Q59-T369, 4 Å)[30] between Cα5 and H1 helices. While in the closed state of the AHD domain, an additional CH_3-π interaction between F376 and M60 plays a significant role (Fig.4d and Figs.4g-i). Of note, in all complex structure resolved so far, the crystallographic complex structure of β2AR-Gαβγ represents the sole fully activated complex structure, in which the AHD domain with an open of 88° while all others are between 55-65°. This could be the effect from crystallographic packing in the crystallization process [31]. Collectively, these findings provide a molecular basis for the limited nucleotide exchange observed in the intermediate GPCR-G protein complex.

Discussion

Previous MD simulation has indicated that GTPγS and GDP exhibited different contact patterns with G protein[32]. A recent study also demonstrated a transition process of GTP nucleotide in a β_2AR-regulated G protein from a “loose” interaction site to the final nucleotide-binding pocket by 2 Å[33]. Our study provides evidence for a 2 Å distance dislocation of nucleotide, regulated by a “lift” of the Cα5 tail by 2 Å, which is essential for dislodging the AHD domain of the G protein from the Ras-like domain. This facilitates the opening of the canonical site 2, accommodating GTP for free-nucleotide exchange and hydrolysis[34]. However, the precise location of site 1 en route from the S4-Gαβγ to the S5-Gαβγ in the GPCR activation process and its specific functional role in G protein signaling remain unclear and require further characterization in the future.

282 GPCR activation is known to involve the transition through multi-states[4-12]. However,
283 transient intermediate states represent higher energy substates from energy landscape
284 perspective and are thus challenging to characterize, especially with regard to obtaining
285 transient GPCR-G protein complexes and studying their functions. Our current study
286 demonstrates a strategy whereby intermediate conformational states can be identified by
287 ^{19}F-qNMR, trapped by point mutation, and structurally and functionally characterized in
288 their complexes with G proteins. Although we used $A_{2a}R$ as a model system, it is clear
289 that such strategy of utilizing 19F-qNMR-guided cryo-EM, in which 19F-NMR serves as
290 conformational indicator, can be broadly applied to study transient complexes of other
291 GPCRs and proteins of interest during activation or inhibition processes. Deciphering the
292 functions of intermediate states and their complexes enables a comprehensive
293 understanding of GPCR signaling complexity and the exploration of alternative
294 therapeutic approaches by targeting a specific disease-related conformation(complex).
295 As the advance of our knowledge on structures and functions of individual conformational
296 states and their complexes, it will become possible to design drug based on their
297 conformational selectivity on the receptor, considering signaling bias originated from
298 conformational bias [5].
299
300
301
302
303
304
305
306
307
308
309
310
311
312

313 **Figures and Legends**

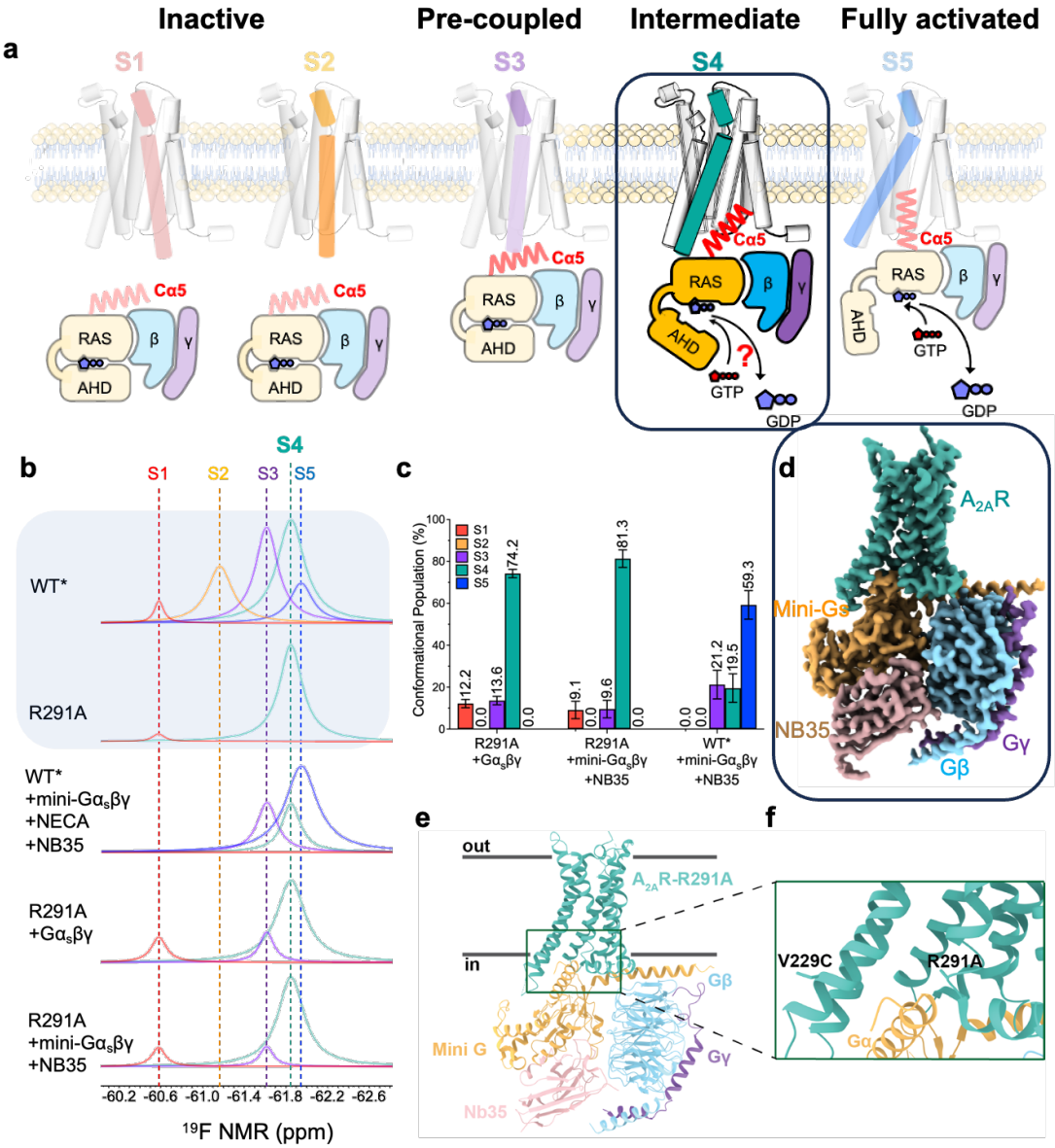

Fig.1: Identification of the intermediate complex investigated in this study. a, Proposed activation model of GPCR, including inactive states S1 and S2, pre-coupled complex (S3-G$\alpha_s\beta\gamma$), intermediate complex (S4-G$\alpha_s\beta\gamma$), and the fully activated complex (S5-G$\alpha_s\beta\gamma$), in which S4-G$\alpha_s\beta\gamma$ was highlighted in teal for this study. **b,** In reference to Extended Data Fig. 1, the deconvoluted conformational profiles probed by ^{19}F-qNMR for the R291A construct were presented as a function of G$\alpha_s\beta\gamma$ and mini-G$\alpha_s\beta\gamma$. ^{19}F-qNMR spectra of WT* and R291A were used as the benchmarks for S1 through S5, adapted from the reference (Wang et al, 2023, Nature Commun). The spectrum of WT*+mini-G$\alpha_s\beta\gamma$+NECA+NB35 represents the feature for PDB: 6GDG. **c,** The population distributions of conformational states for R291A+mini-G$\alpha_s\beta\gamma$+NB35, R291A+G$\alpha_s\beta\gamma$, and WT*+mini-G$\alpha_s\beta\gamma$+NB35 (S5-G$\alpha_s\beta\gamma$). The SD values were determined based on spectral S/Ns and fitting errors of the deconvolutions. **d,** Ribbon representation of S4-mini-G$\alpha_s\beta\gamma$. **e,** Highlighted interfacial section of S4-mini-G$\alpha_s\beta\gamma$. **f**, cryo-EM density map of intermediate S4-mini-G$\alpha_s\beta\gamma$ complex.

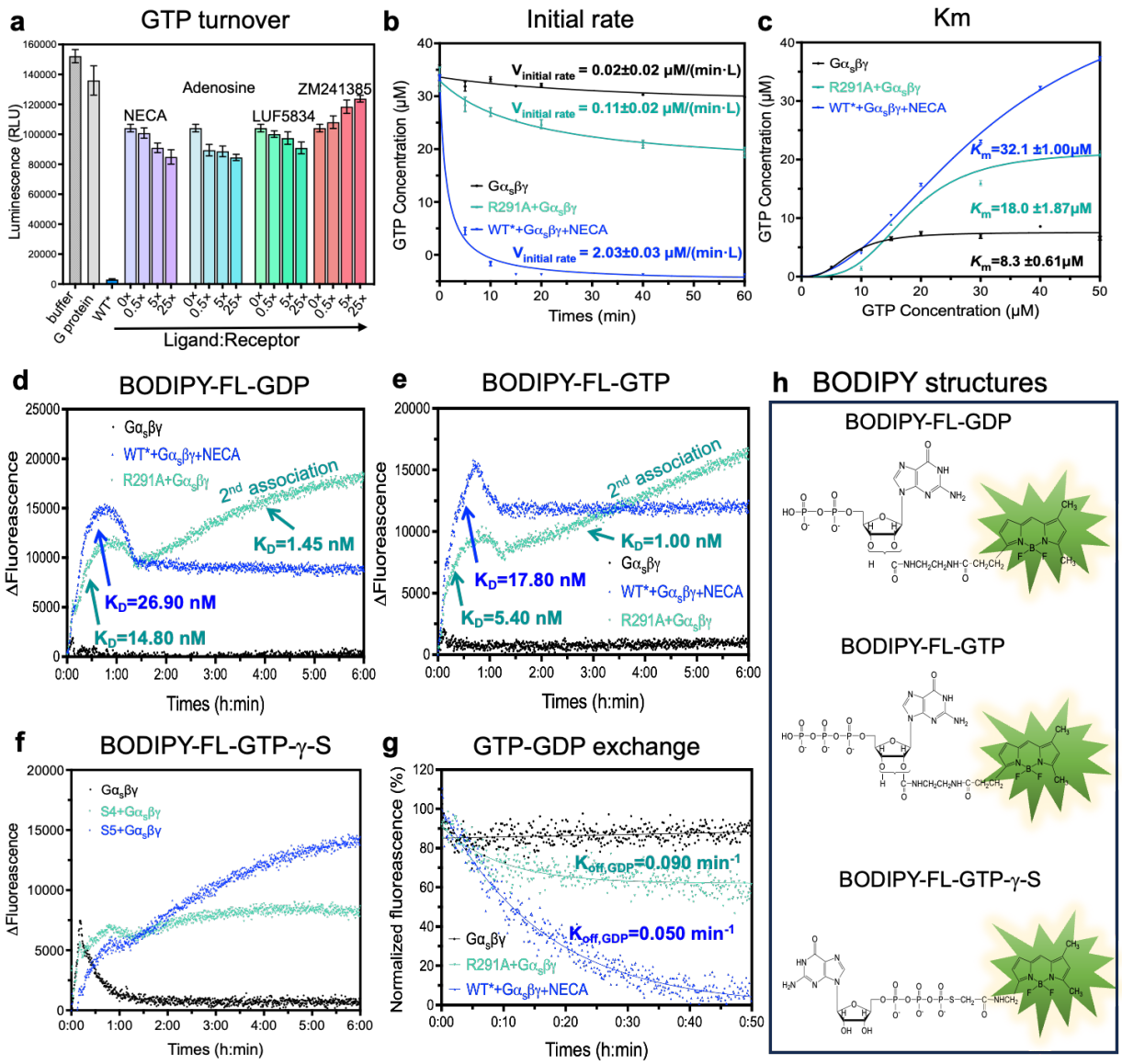

Fig. 2: S4 mediated GTP hydrolysis and nucleotide exchange. a, GTP hydrolysis of the S4 mediated $G\alpha_s\beta\gamma$ as a function of inverse, partial, and full agonists, in reference to $G\alpha_s\beta\gamma$ alone (negative control) and the S5 mediated $G\alpha_s\beta\gamma$ (positive control). **b,** Time course of GTP hydrolysis of the S4 mediated $G\alpha_s\beta\gamma$, in reference to $G\alpha_s\beta\gamma$ alone (negative control) and the S5 mediated $G\alpha_s\beta\gamma$ (positive control); the initial rate of each catalysis was also calculated as presented. **c,** Km values for S4 mediated $G\alpha_s\beta\gamma$, in reference to $G\alpha_s\beta\gamma$ alone (negative control) and the S5 mediated $G\alpha_s\beta\gamma$ (positive control). **d,** BODIPY-FL-GDP binding assay. **e,** BODIPY-FL-GTP binding assay. **f**, BODIPY-FL-GTP-γ-S binding assay **g,** GTP-GDP exchange rate comparison. **g**, The structures of BODIPY-FL-GDP, BODIPY-FL-GTP, and BODIPY-FL-GTP-γ-S.

317

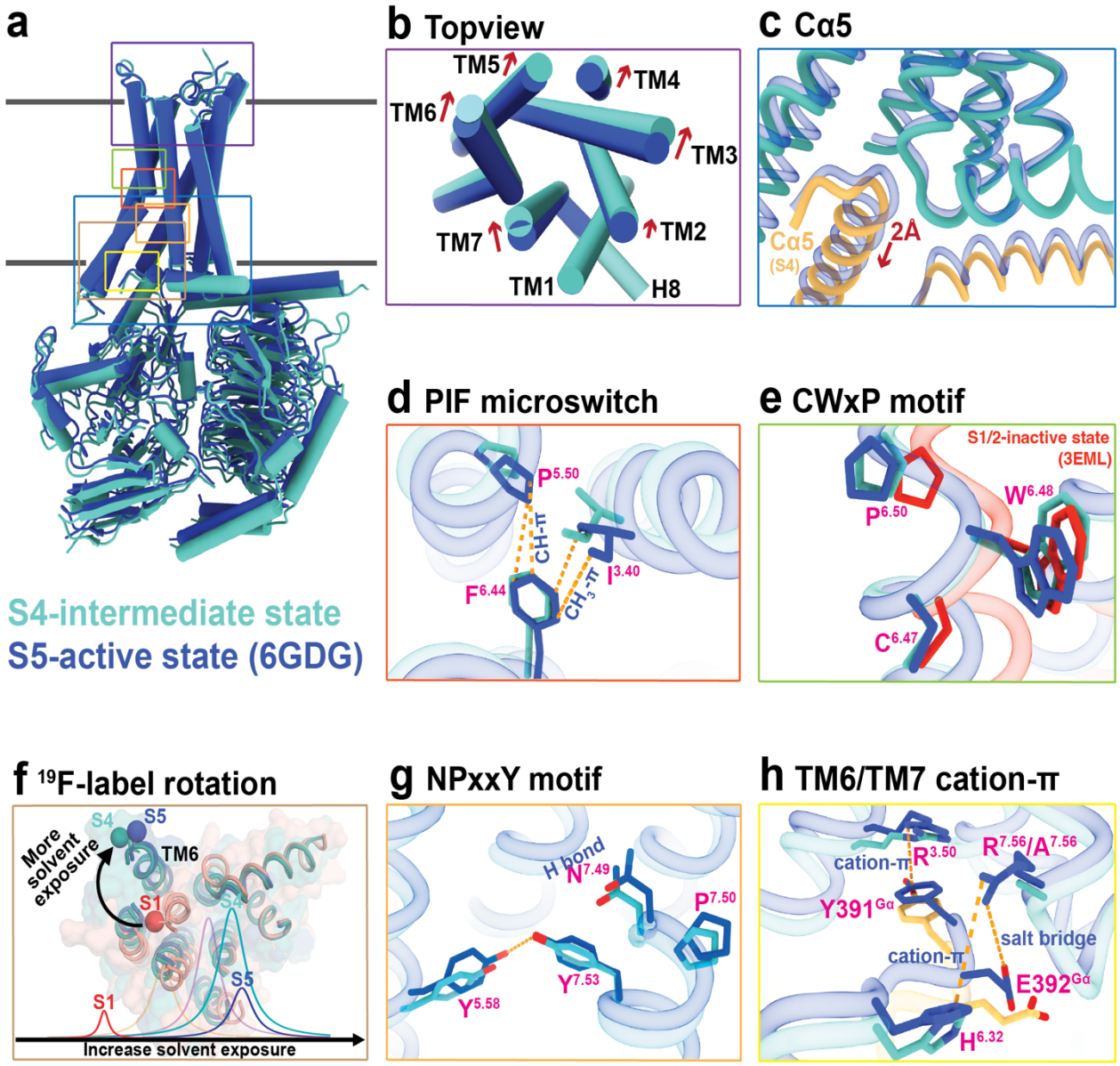

Fig. 3: Structural features of the receptor in intermediate complex. a, Superimposed cylinder representations of S4-mini-G$\alpha_s\beta\gamma$ and S5-mini-G$\alpha_s\beta\gamma$. **b,** Top view of ligand binding domain of the S4 state compared to the S5 state. **c**, Cα5 motion of Gα_s. **d**, PIF microswitch. **e**, CWxP motif. **f**, ^{19}F-tag rotation, and corresponding NMR spectrum. **g,** NPxxY motif. **h**, TM6 and TM7 cation-π interaction in two complexes.

318

319

320

321

322

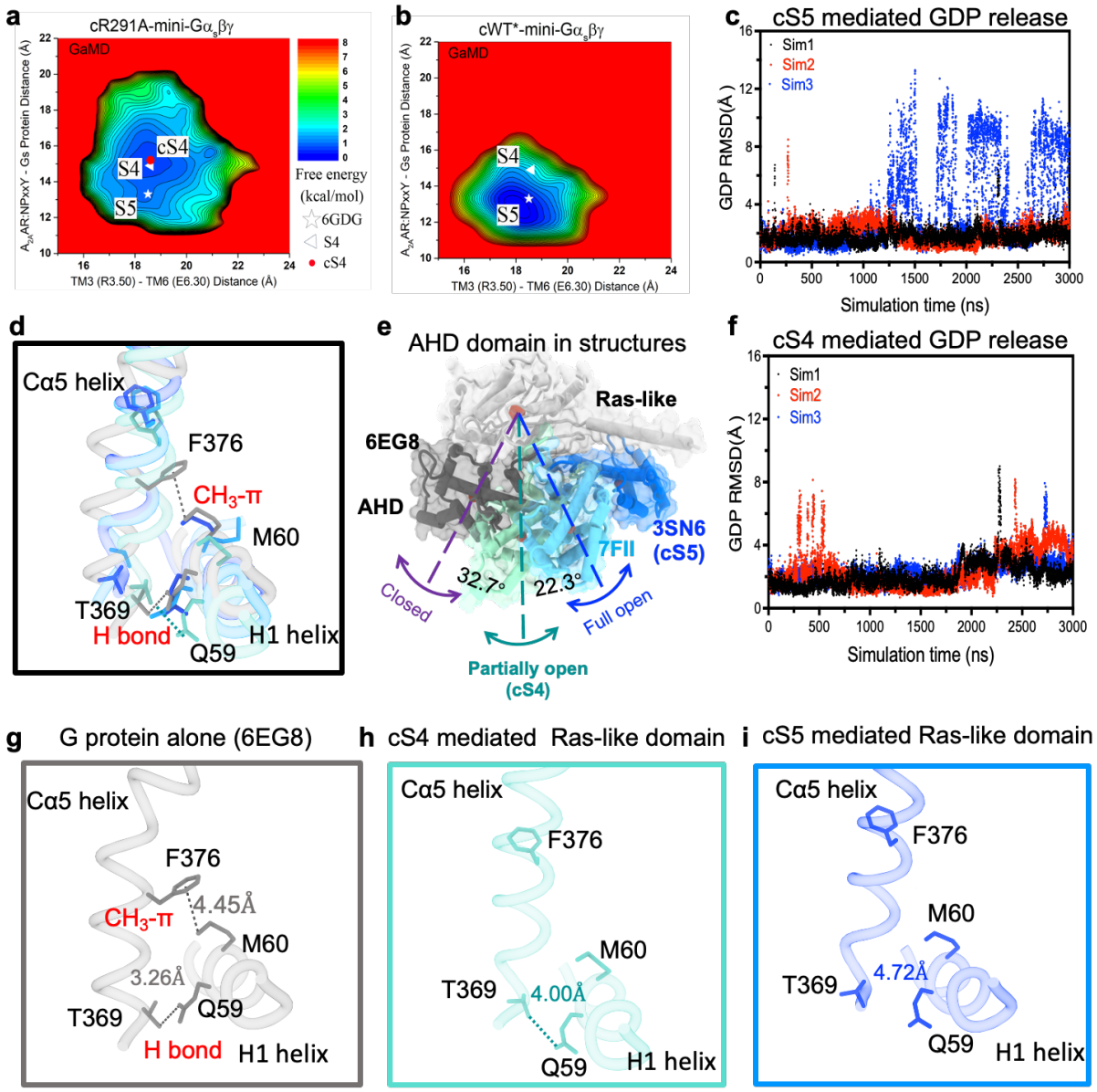

Fig. 4: Structural features of $A_{2A}R$ and G protein in GaMD simulation. a, 2D free energy profiles of the cR291A-mini-Gαsβγ complex system. **b**, 2D free energy profiles of the cWT*-mini-Gαsβγ complex systems. The white triangle and asterisk indicate cryo-EM structures of the S5 and S4 states, respectively. **c**, Root-mean square deviation (RMSD) of GDP relative to the initial position in the GaMD simulation for cS5 mediated G protein. **d**, Superimposed positions of Cα5 and H1 helices when G protein is inactive, partial activated, and fully activated. **e**, The positions of AHD domain when G protein is inactive, partial activated, and fully activated. **f**, RMSD of GDP relative to the initial position in the GaMD simulation for cS4 mediated G protein. **g-i**, The relative positions of Cα5 and H1 helices when G protein is inactive (6EG8), partial activated (cS4 mediated), and fully activated (cS5 mediated).

323

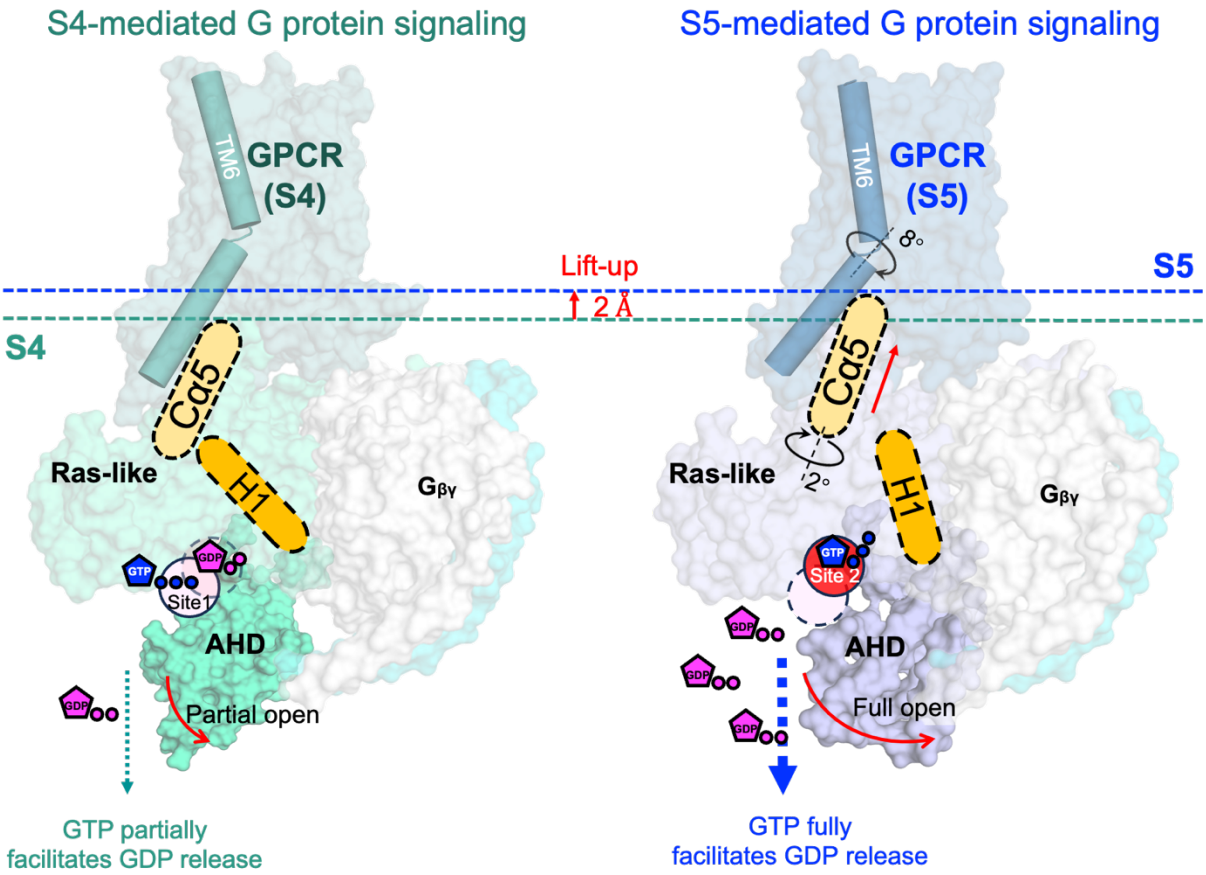

Figure 5: A limited nucleotide exchange model for intermediate GPCR-Gα$_s$βγ complex. In the S5-mediated Gα the interaction between Cα5 and H1 helices was interrupted while this interaction is partially maintained through a weakened H-bond between Cα5 and H1 helices in Ras-like domain.

335 **Methods**

336

337 **Plasmid construction and transformation**

338 The full-length human $A_{2A}R$ gene, originating from construct pPIC9K_ADORA2A, was
339 generously provided by Prof. Takuya Kobayashi (Kyoto University, Kyoto, Japan). The C-
340 terminally truncated construct $A_{2A}R$_316, constructed in our previous study, has an
341 integrated FLAG tag on the N-terminus and a poly-his tag on the C-terminus[7]. Based on
342 this construct, the mutations V229C and R291A were described elsewhere[13]. All
343 constructs were sequenced by a facility at Eurofins genomics, with the AOX1 primer pair
344 of PF_{AOX1} and PR_{AOX1}. Freshly prepared competent cells of strain *Pichia Pastoris* SMD
345 1163 (*Δhis4 Δpep4 Δprb1,* Invitrogen) were electro-transformed with *Pme*I-HF (New
346 England Biolabs) linearized plasmids containing different mutant genes using a Gene
347 Pulser II (Bio-Rad). High-copy clone selection was performed using an in-house protocol
348 described previously[8,35]. A high-yield construct was then screened by an immunoblotting
349 assay with both anti-FLAG and anti-Poly-his for further large-scale expression screening.

350

351 **Receptor expression, purification, and labeling**

352 The screened WT* and mutants R291A, were pre-cultured on YPD [1% (w/v) yeast
353 extract, 2% (w/v) peptone and 2% (w/v) glucose] plates containing 0.1 mg/mL G418. A
354 single colony for each construct was inoculated into 4 mL YPD medium and cultured at
355 30 °C for 12 hours, then transferred into 200 mL BMGY medium [1% (w/v) yeast extract,
356 2% (w/v) peptone, 1.34% (w/v) YNB (yeast nitrogen base) without amino acids, 0.00004%
357 (w/v) biotin, 1% (w/v) glycerol, 0.1 M PB (phosphate buffer) at pH 6.5] and cultured at
358 30 °C for another 30 h. The cells were then transferred into 1 L of BMMY medium [1%
359 (w/v) yeast extract, 2% (w/v) peptone, 1.34% (w/v) YNB without amino acids, 0.00004%
360 (w/v) biotin, 0.5% (w/v) methanol, 0.1 M phosphate buffer at pH 6.5, 0.04% (w/v) histidine
361 and 3% (v/v) DMSO, 10 mM theophylline] at 20 °C. 0.5% (v/v) methanol was added every
362 12 h. 60 h after induction by methanol, cells were harvested for purification.

363

364 The cell pellets were collected by centrifugation at 4,000 ×g for 20 minutes and washed
365 one time with washing buffer (50 mM HEPES, 10% glycerol, pH 7.4) before the addition

366 of breaking buffer (50 mM HEPES, pH 7.4, 100 mM NaCl, 2.5 mM EDTA, 10% glycerol)
367 in a ratio of 4:1 (buffer: cells). The resuspended cell pellets were subject to disruption 3
368 times using a Microfluidizer at a pressure of 20,000 psi. Intact cells and cell debris were
369 separated by low-speed centrifugation (8,000 ×g) for 30 minutes. The supernatant was
370 collected and centrifuged at 100,000 ×g for 2 h, and the precipitated cell membrane was
371 then immediately dissolved in membrane lysis buffer (50 mM HEPES, pH 7.4, 100 mM
372 NaCl, 0.5% LMNG-3 (Lauryl Maltose Neopentyl Glycol) and 0.1% CHS (cholesteryl
373 hemisuccinate)) with rotation 2 h or overnight at 4 °C until the membrane was dissolved.
374 Subsequently, Talon resin (Clontech) was added to the solubilized membranes and
375 incubated for at least 2 h or overnight under gentle agitation.
376
377 The $A_{2A}R$-bound Talon resin was washed twice with a buffer of 50 mM HEPES, pH 7.4,
378 100 mM NaCl, 0.02% LMNG-3 and 0.002% CHS and resuspended in the same buffer.
379 The $A_{2A}R$-bound Talon resin was then resuspended in buffer made of 50 mM HEPES, pH
380 7.4, 100 mM NaCl, 0.02% LMNG-3 and 0.002% CHS, and combined with 10-20 fold
381 excess of the NMR label (2-bromo-*N*-(4-(trifluoromethyl)phenyl)acetamide, BTFMA,
382 Apollo Scientific, Stockport, UK) under gentle agitation overnight at 4 °C. Another aliquot
383 of NMR label was then added and incubated for an additional 6 h to ensure complete
384 labeling. The $A_{2A}R$-bound Talon resin was washed in a disposable column extensively
385 with buffer containing 50 mM HEPES, pH 7.4, 100 mM NaCl, 0.02% LMNG-3 and 0.01%
386 CHS, and apo $A_{2A}R$ was then eluted from the Talon resin with 50 mM HEPES, pH 7.4,
387 100 mM NaCl, 0.02% LMNG-3 and 0.01% CHS, 250 mM imidazole and concentrated to
388 a volume of 5 mL. The XAC-agarose gel and $A_{2A}R$ were then incubated together for 2 h
389 under gentle agitation. The functional $A_{2A}R$ was eluted with 50 mM HEPES, pH 7.4, 0.02%
390 LMNG-3, 0.002% CHS, 100 mM NaCl, 20 mM theophylline. The eluted samples were
391 concentrated to 1 mL by centrifugal filtration (MWCO, 3.5 KDa), and an extensive dialysis
392 was performed to remove the XAC in the sample. The functional apo $A_{2A}R$ was then
393 prepared for NMR. All receptors described in this manuscript were purified using poly-his
394 resin followed with a ligand-column, in which the $A_{2A}R$ antagonist xanthine amine
395 congener (XAC) was conjugated to Affi-Gel 10 activated affinity media.
396

397 **Preparation of mini-G$\alpha_s\beta\gamma$ heterotrimer**

398 The plasmid for mini-Gα_s399 was generously provided by Drs. Christopher G. Tate from
399 MRC Laboratory of Molecular Biology, Cambridge and Javier García Nafría from Institute
400 for Biocomputation and Physics of Complex Systems (BIFI) and Laboratorio de
401 Microscopías Avanzadas (LMA), University of Zaragoza. It was expressed in the *E. coli*
402 strain BL21(DE3). Cells were collected by centrifugation at 4,000 ×g for 20 min and lysed
403 by sonication. After another centrifugation, the supernatant was purified by Talon resin.
404 The sample was loaded into a HiLoad16/60 column to obtain purified mini-Gα_s protein.
405 The purified protein was concentrated to 3 mg/mL and flash frozen in liquid nitrogen and
406 stored at -80 °C for further use. The expression and purification of the respective
407 components and assembly to make the complex containing mini-G$\alpha_s\beta_1\gamma_2$, and the
408 preparation of nanobody Nb35, were all performed following the protocols described
409 previously [1,36,37].

410

411 **^{19}F NMR experiments**

412 NMR samples typically consisted of 280-300 μL volumes with 20-50 μM $A_{2A}R$ in 50 mM
413 HEPES buffer and 100 mM NaCl, doped with 10% D_2O. The receptor was stabilized in
414 0.02% LMNG-3 and 0.002% CHS. All ^{19}F NMR experiments were performed on a 600
415 MHz Varian Inova spectrometer using a ^{19}F dedicated resonance probe. Typical
416 experimental setup included a 16 μs 90° excitation pulse, an acquisition time of 200 ms,
417 a spectral width of 15 kHz, and a repetition time of 1 s. Most spectra were acquired with
418 15,000-50,000 scans. Processing typically involved zero filling, and exponential
419 apodization equivalent to 15 Hz line broadening.

420

421

422 **GTPase hydrolysis assay**

423 The GTPase hydrolysis assay was analyzed using a modified protocol of the GTPase-
424 Glo™ assay (Promega)[38]. The reaction was started by mixing 300 nM G$\alpha_s\beta\gamma$ with the
425 purified receptors in varied concentrations with a final volume of 10 μL in the buffer
426 containing 50 mM HEPES, pH 7.4, 100 mM NaCl, 0.002% CHS, 0.02% LMNG-3. For the
427 GTP hydrolysis capacity of the S4 state as a function of ligand measurement, 5x and 25x

428 ligand compared to receptor concentration was added. After 30 min incubation at room
429 temperature, 10 μL 2xGTP-GAP solution containing 10 μM GTP, 1 mM DTT and the
430 cognate GAP was added to each well, followed with a 120 min incubation at room
431 temperature. For the Michaelis–Menten constant measurement, the 2xGTP-GAP solution
432 containing 5-50 μM GTP was used. Then, 20 μL reconstituted GTPase-Glo™ reagent
433 containing 5 μM ADP was added to each sample and incubated for another 30 min at
434 room temperature with shaking. Luminescence was measured following the addition of
435 40 μL detection reagent and incubation for 10 min at room temperature using a BioTEK-
436 Flx800 plate reader at 528±20 nm. Determine the amount of GTP consumed in a
437 biochemical reaction by referencing a standard curve that relates light units (RLU)
438 indicative of product formation to GTP concentration. Using this data, calculate the rate
439 of the enzymatic reaction (velocity, v) by applying the Michaelis-Menten equation: $v =$
440 $V_{max}/(1+(K_m/[S]))$. To facilitate the determination of V_{max} and K_m, construct a Lineweaver-
441 Burk plot, which linearizes the relationship by graphing the reciprocal of the velocity ($1/v$)
442 against the reciprocal of the substrate concentration ($1/[S]$). The calculations of initial
443 rates were performed at 1.08 min in the linear reaction phase of catalysis. Analysis of
444 data was performed by Excel and GraphPad Prism® 9.0.
445
446 **BODIPY-FL-GTP, BODIPY-FL-GDP binding, and nucleotide exchange**
447 The nucleotide-binding assay utilized BODIPY-FL-GTP and BODIPY-FL-GDP, from
448 Invitrogen™, each supplied as a mixture of two isomers with the fluorophore attached at
449 either the 2′ or 3′ position on the ribose ring. BODIPY-FL-GTP could be hydrolyzed to
450 BODIPY-FL-GDP. To form the GPCR-G protein complex, a solution containing 2 μM G
451 protein and 100 μM receptor was incubated for 30 minutes at 22°C. The fully activated
452 state of the WT* receptor was achieved by supplementing the mixture with 10 mM NECA.
453 Assays were conducted at 22°C using 96-well half-area microtiter plates in a BioTek plate
454 reader, with excitation at 475 nm and emission measured at 528 nm. The assay buffer
455 comprised 20 mM HEPES (pH 7.4), 1 mM EDTA, and 10 mM $MgCl_2$, supplemented with
456 0.01% LMNG-3 for protein stability. Initial kinetic data were acquired for 100 nM BODIPY-
457 FL-GTP/BODIPY-FL-GDP in the absence of G protein for 70 seconds to establish a
458 baseline fluorescence intensity. Subsequently, 200 nM heterotrimer G proteins, with or

459 without the receptor, were added, and mixing was rapidly performed in the fluorescence
460 cuvette. Data collection proceeded uninterrupted, and resulting kinetics spectra were
461 plotted and fitted to a one-phase association function using GraphPad Prism 9.0. For the
462 GTP-GDP exchange assay, the GPCR-G protein complex was formed as described,
463 followed by incubation with 100 nM BODIPY-FL-GDP for 2 hours. Baseline fluorescence
464 intensity was measured for 70 seconds using the plate reader, after which 1 μM GTP (in
465 a concentration of 10×GDP), procured from Invitrogen™, was added to facilitate the
466 exchange of BODIPY-FL-GDP to GTP. All experiments were repeated three times, and
467 resulting kinetics spectra were analyzed using GraphPad Prism 9.0.
468
469 **Gaussian accelerated molecular dynamics (GaMD)**
470 GaMD is an enhanced sampling method that works by adding a harmonic boost potential
471 to reduce the system energy barriers [39,40]. When the system potential $V(\vec{r})$ is lower than
472 a reference energy E, the modified potential $V^*(\vec{r})$ of the system is calculated as:

473 $$V^*(\vec{r})=V(\vec{r})+\Delta V(\vec{r})$$

474 $$\Delta V(\vec{r})=\begin{cases}\frac{1}{2}k\left(E-V(\vec{r})\right)^2, & V(\vec{r})<E\\ 0, & V(\vec{r})\geq E,\end{cases} \quad (1)$$

475 where *k* is the harmonic force constant. The two adjustable parameters E and k are
476 automatically determined on three enhanced sampling principles. First, for any two
477 arbitrary potential values $v_1(\vec{r})$ and $v_2(\vec{r})$ found on the original energy surface, if
478 $V_1(\vec{r})<V_2(\vec{r})$, ΔV should be a monotonic function that does not change the relative order
479 of the biased potential values; i.e., $V_1^*(\vec{r})<V_2^*(\vec{r})$. Second, if $V_1(\vec{r})<V_2(\vec{r})$, the potential
480 difference observed on the smoothened energy surface should be smaller than that of the
481 original; i.e., $V_2^*(\vec{r})-V_1^*(\vec{r})<V_2(\vec{r})-V_1(\vec{r})$. By combining the first two criteria and plugging in
482 the formula of $V^*(\vec{r})$ and ΔV, we obtain

483 $$V_{max}\leq E\leq V_{min}+\frac{1}{k}, \quad (2)$$

484 Where V_{min} and V_{max} are the system minimum and maximum potential energies. To
485 ensure that Eq. 2 is valid, *k* has to satisfy: $k\leq 1/(V_{max}-V_{min})$. Let us define: $k=k_0\cdot 1/(V_{max}-$
486 $V_{min})$, then $0<k_0\leq 1$. Third, the standard deviation (SD) of ΔV needs to be small enough
487 (i.e. narrow distribution) to ensure accurate reweighting using cumulant expansion to the

488 second order: $\sigma_{\Delta V}=k(E-V_{avg})\sigma_V \leq \sigma_0$, where V_{avg} and σ_V are the average and SD of
489 $\Delta V$with σ_0 as a user-specified upper limit (e.g., $10k_BT$) for accurate reweighting. When E
490 is set to the lower bound $E=V_{max}$ according to Eq. 2, k_0 can be calculated as

491 $$k_0 = \min(1.0, k_0') = \min\left(1.0, \frac{\sigma_0}{\sigma_V} \cdot \frac{V_{max}-V_{min}}{V_{max}-V_{avg}}\right), \quad (3)$$

492 Alternatively, when the threshold energy E is set to its upper bound $E=V_{min}+1/k$, k_0 is set
493 to:

494 $$k_0 = k_0'' \equiv \left(1-\frac{\sigma_0}{\sigma_V}\right) \cdot \frac{V_{max}-V_{min}}{V_{avg}-V_{min}}, \quad (4)$$

495 If $k_0''$is calculated between 0 and 1. Otherwise, k_0 is calculated using Eq. 3.
496

497 **System setup and simulation analysis**

498 The cryo-EM structure of wild-type NECA-bound $A_{2A}R$ bound by mini-$G\alpha_s$ (PDB ID:
499 6GDG[16]) was used for setting up simulation systems of the wild-type NECA-bound cWT*-
500 $A_{2A}R$-mini-$G\alpha_s\beta\gamma$, *apo* cR291A-mini-$G\alpha_s\beta\gamma$, *apo* cWT*-$A_{2A}R$-$G\alpha_s\beta\gamma$ and *apo* cR291A-
501 $G\alpha_s\beta\gamma$. The missing residues in the extracellular loop 2 (ECl2) and intracellular loop 3
502 (ICL3) of the receptor were modelled with Swiss-Modeller[41]. For the *apo* cR291A-mini-
503 $G\alpha_s\beta\gamma$, the simulation structure was generated by mutanting the correspoding R291A and
504 V229C in the wild-type system and deleting the agonist NECA. To build the wild-type *apo*
505 $A_{2A}R$ bound by the full-length of Gs protein (*apo* cWT*-$A_{2A}R$-$G\alpha_s\beta\gamma$), the Swiss-Modeller[41]
506 was used to build the Gs protein with a geometry and orientation similar to the Gs protein
507 in the fully active state of the β_2AR-Gs complex (PDB ID: 3SN6[1]). The coordinates of the
508 GDP and Mg^{2+} were obtained by aligning the Ras domain of the crystal structure of Gs-
509 bound GDP (PDB ID: 6AU6[42]) to the modelled full-length Gs protein bound by the
510 $A_{2A}R$.The simulation structure of the *apo* cR291A-$G\alpha_s\beta\gamma$ was generated by substituting
511 residues Arg291 and Val232 in the wild-type system (*apo* cWT*-$A_{2A}R$-$G\alpha_s\beta\gamma$) with Ala and
512 Cys, respectively.

513

514 VMD was used to insert the NECA-bound cWT*-$A_{2A}R$-mini-$G\alpha_s\beta\gamma$, *apo* cR291A-mini-
515 $G\alpha_s\beta\gamma$, *apo* cWT*-$A_{2A}R$-$G\alpha_s\beta\gamma$, and *apo* cR291A-$G\alpha_s\beta\gamma$ complex into POPC (palmitoyl-2-

516 oleoyl-sn-glycero-3-phosphocholine) lipids to prepare simulation systems. In each
517 simulation system, the protein and lipid bilayer were solvated with TIP3P water molecules
518 in a box of 11.2 nm x 13.1 nm x 14.6 nm with the periodic boundary condition. The system
519 charge was neutralized with 150 mM NaCl. The CHARMM36m parameter set[43-45] was
520 used for the proteins and lipids, and Guanosine diphosphate (GDP). Force field
521 parameters of the NECA agonist were obtained from the ParamChem web server[46]. The
522 four simulation systems were first energy minimized for 5,000 steps with constraints on
523 the heavy atoms of the proteins and phosphor atom of the lipids. The hydrogen-heavy
524 atom bonds were constrained using the SHAKE algorithm and the simulation time step
525 was set to 2.0 fs. The particle mesh Ewald (PME) method[47] was employed to compute
526 the long-range electrostatic interactions and a cutoff value of 9.0 Å was applied to treat
527 the non-bonded atomic interactions. The temperature was controlled using the Langevin
528 thermostat with a collision frequency of 1.0 ps^{-1}. The system was then equilibrate using
529 the constant number, volume, and temperature (NVT) ensemble at 310K for 250 ps and
530 under the constant number, pressure, and temperature (NPT) ensemble at 310 K and 1
531 bar for another 1 ns with constraints on the heavy atoms of the protein, followed by 10 ns
532 short conventional MD (cMD) without any constraint.

533

534 The GaMD module implemented in the GPU version of AMBER22[48-50] was then applied
535 to perform the simulations of NECA-bound cWT*-A_{2A}R-mini-G$\alpha_s\beta\gamma$, *apo* cR291A-mini-
536 G$\alpha_s\beta\gamma$, *apo* cWT*-A_{2A}R-G$\alpha_s\beta\gamma$, and *apo* cR291A-G$\alpha_s\beta\gamma$. GaMD simulations included a 8-
537 ns short cMD run used to collect the potential statistics for calculating GaMD acceleration
538 parameters, an 56-ns GaMD equilibration after adding the boost potential, and finally
539 three independent 2,000-ns GaMD production simulations with randomized initial atomic
540 velocities for the systems of the NECA-bound cWT*-A_{2A}R-mini-G$\alpha_s\beta\gamma$ and *apo* cR291A-
541 A_{2A}R-mini-G$\alpha_s\beta\gamma$ complex, and 3,000-ns GaMD production simulations for the systems of
542 *apo* cWT*-A_{2A}R-G$\alpha_s\beta\gamma$ and *apo* cR291A-G$\alpha_s\beta\gamma$ with randomized initial atomic velocities.
543 The average and SD of the system potential energies were calculated every 800,000
544 steps (1.6 ns). All GaMD simulations were performed at the “dual-boost” level by setting
545 the reference energy to the lower bound. One boost potential was applied to the dihedral

546 energetic term and the other to the total potential energetic term. The upper limit of the
547 boost potential SD, σ_0 was set to 6.0 kcal/mol for both the dihedral and the total potential
548 energetic terms.

549

550 For each simulation system, all three GaMD production trajectories were combined
551 together for analysis with CPPTRAJ[51]. The distance between the NPxxY motif of the
552 receptor and the last five residues of $G\alpha_s$ α5 helix (A_{2A}AR:NPxxY-$G\alpha_s$:α5 distance), the
553 distance between the receptor TM3 and TM6 intracellular ends (measured by the distance
554 between the Cα atoms of receptor residues Arg102$^{3.50}$ and Glu228$^{6.30}$), the root-mean-
555 square derivation of GDP (GDP RMSD) relative to the simulation starting structure were
556 selected as reaction coordinates. The angle between the Ras domain and α helical
557 domain (AHD) was used as another reaction coordinate to indicate their relative
558 orientation, which was defined by the two vectors of $G\alpha_s$ AHD and $G\alpha_s$ Ras domain. Vector
559 1 went through the $G\alpha_s$ AHD and A161 centers and vector 2 went through $G\alpha_s$ Ras domain
560 and E299 centers. The PyReweighting[52] toolkit was applied to reweight GaMD
561 simulations to recover the original free energy profiles of the simulation systems. 2D free
562 energy profiles were computed using the combined trajectories from all the three
563 independent GaMD simulations for each system with the A_{2A}R:NPxxY-$G\alpha_s$:α5 distance,
564 TM3-TM6 distance, GDP RMSD and the angle between the Ras domain and AHD as
565 reaction coordinates. A bin size of 1.0 Å was used for the A_{2A}R:NPxxY-$G\alpha_s$:α5 distance,
566 TM3-TM6 distance and GDP RMSD. A bin size of 6.0° was used for the angle between
567 the Ras domain and AHD as reaction coordinate. The cutoff was set to 500 frames for 2D
568 free energy calculations.

569

570 **Preparation of the A_{2A}R-mini-$G_S\beta_1\gamma_2$-Nb35 complex**

571 A_{2A}R, mini-G_S-$\beta_1\gamma_2$ and Nb35 were mixed in a molar ratio of 1:2:4, to yield a final complex
572 concentration of 1 mg/mL. To this mixture, 0.1 U of apyrase was added, followed by an
573 overnight incubation at 4°C. The mixture was then concentrated with a 100 kDa MWCO
574 Amicon filter and injected onto a Superdex200 Increase 10/300 GL gel filtration column
575 equilibrated with buffer (50 mM HEPES, 100 mM NaCl, 0.002% LMNG-3, 0.0002% CHS

576 (w/v)). Monodisperse fractions were concentrated with a 100 kDa MWCO Amicon filter
577 immediately prior to cryo-EM grid preparation.
578
579 Negative staining of the complex was performed with 0.75% uranium formate, following
580 an established protocol[53].Grids were examined using an FEI T12 microscope operated at
581 120 kV, and images were recorded using a 4K x 4K charge-coupled device (CCD) camera
582 (UltraScan 4000, Gatan).
583
584 **Cryo-EM sample preparation and data acquisition**
585 Freshly prepared A_{2A}R-mini-G_S-$\beta_1\gamma_2$-Nb35 complex at a final concentration of 1 mg/mL,
586 was applied to glow-discharged gold grids coated with either holey carbon film (Quantifoil,
587 300 mesh 1.2/1.3, Au) or holey gold film (UltrAuFoil, 300, mesh 1.2/1.3). These grids were
588 then plunge-frozen using a Vitrobot Mark IV with a blotting time of 4 s and blotting force
589 of 0, at 4 °C and 100% humidity. Grids were subsequently examined and screened using
590 an FEI Tecnai Arctica operated at 200 kV and equipped with an XFEG and a Gatan K3
591 camera. Cryo-EM data collection was performed on a Titan Krios at the UCSF Cryo-EM
592 Center for Structural Biology, operated at an acceleration voltage of 300 kV, equipped
593 with an XFEG, a BioQuantum energy filter (slit width set to 20 eV) and a K3 camera
594 (Gatan).
595
596 All cryo-EM datasets were collected using SerialEM[54]. A multishot collection (3x3 arrays)
597 was employed, incorporating beam-tilt compensation and maximum image shift is 3.5
598 micros. All images were acquired with a nominal magnification of 105 K, resulting in a
599 super-resolution pixel size of 0.4175 Å (physical pixel size of 0.835 Å). Defocus range
600 was set from -0.8 µm to -1.8 µm. A total of 8,805 images were collected, each was dose-
601 fractionated into 80 movie frames with a total exposure time of 2.024 s, resulting in a total
602 fluence of approximately 47.7 electrons per $Å^2$. Data collection statistics are shown in
603 Supplementary Table 1.
604
605 **Image process**

606 A total of 8,805 movie stacks were motion-corrected, dose-weighted, and binned by
607 Fourier cropping to the physical pixel size of 0.835 Å on-the-fly using MotionCor2[55].
608 Motion-corrected, does-weighted sums were used for contrast transfer function (CTF)
609 determination and resolution estimation in cryoSPARC[56]. 424,536 particles were picked
610 from randomly selected 500 micrographs using cryoSPARC blob picker with a diameter
611 of 80-150 Å. These particles were subjected to ab-initio reconstruction and multi-round
612 heterogenous refinement. One class with distinct features of $A_{2A}R$ bound to mini-$G\alpha_s\beta_1\gamma_2$-
613 Nb35 was identified, from which 16 different projection images were created for template
614 picking, yielding 7,282,317 particles from all micrographs.
615
616 After removing junk particles by extensive 2D classifications, 2,328,810 particles were
617 selected for ab-initio reconstruction and multi-round heterogenous refinement. One
618 distinct class of 307,568 particles was identified for further non-uniform refinement of the
619 $A_{2A}R$-mini-$G\alpha_s\beta_1\gamma_2$-Nb35 complex, yielding a reconstruction with a global resolution of
620 3.04Å. This particle stack was then exported to RELION[57] for multiple rounds of 3D
621 refinement (initial low-pass filter: 10 Å; mask diameter: 360 Å; reference mask: no) to
622 produce a new reconstruction, from which a mask without the detergent micelle was
623 generated by using the segment map function in Chimera[58] (initial threshold: 0.0001;
624 extend_inimask: 4; width_soft_edge: 4). Particle subtraction function in RELION was
625 applied by using this mask to generate a micelle removed particle stack.
626
627 Next, we applied 3D classification to the micelle subtracted particles with a reference
628 model without micelle (reference mask: generated last step; initial low-pass filter: 10 Å;
629 mask diameter: 260 Å; regularisation parameter T: 3; number of iterations: 50; number of
630 classes: 5; perform local angular searches: no). A new reconstruction of the entire $A_{2A}R$-
631 mini-G_S-$\beta_1\gamma_2$-Nb35 complex from 71,547 particles was identified for further refinement in
632 RELION (initial low-pass filter: 3.5 Å; mask diameter: 260 Å; angular sampling interval:
633 1.8º; local search from auto-sampling: 0.9º). A final 3D reconstruction was calculated in
634 cisTEM[59] with default settings and without further refinement. The numeric resolution was
635 determined from Fourier Shell Correction (FSC) using criterion of FSC = 0.143[60]. The final

636 map was sharpened by DeepEMhancer[61] and used for model building and figure
637 generation.
638
639 **Model building**
640 For model building, the initial model was generated by fitting the existing coordinates of
641 the activated state of A_{2A}R-mini-G_S-$\beta_1\gamma_2$-Nb35 complex (PDB: 6GDG) into our cryo-EM
642 density maps using ChimeraX[62]. Discrepancies between the initial model and the density
643 maps were then manually built and refined ISOLDE[63] and coot[64]. Subsequent refinements
644 were performed in Phenix[65] with secondary structure constraints. The model was
645 validated by wwPDB validation server[66] and no major issues was reported. A summary
646 of the parameters used in data collection and model building is provided in Supplementary
647 Table 1.
648
649
650 **Data representation**
651 All statistical tests such as GTP hydrolysis assessments were conducted using GraphPad
652 Prism 9.0. The central point of all data points gives the mean value with s.d. for all data
653 unless otherwise specified. Visualization of the atomic models (figures and videos) were
654 made using UCSF ChimeraX and PyMoL (The PyMOL Molecular Graphics System,
655 Version 2.0 Schrödinger, LLC.)

656 **Data Availability**
657 The atomic coordinates of intermediate A_{2A}R-mini-$G\alpha_s\beta\gamma$ has been deposited in the
658 Protein Data Bank with ID: 8VM3.
659
660 **Acknowledgements**
661 We thank Drs. Christopher G. Tate and Javier García Nafría for providing the plasmid of
662 mini-G399. We also thank Hiran Malinda Lamabadu Warnakulasurya and Natasha
663 Jaiswal in assistance of GTP hydrolysis measurements, Dr. Hao Wu for technical
664 assistance in cryo-EM data acquisition and advice on data processing and model building,
665 Wooyoung Choi, Will Arnold and Adamo Mancino for their advice and feedback on

figures, and to the members of the Cheng laboratory for helpful discussions. The cryo-EM facility at UCSF is managed by David Bulkley and Glenn Gilbert. Some of this work was performed at the Janelia cryo-EM facility, supported by Howard Hughes Medical Institute (HHMI). Computation at the Cheng laboratory is supported by Chengmin Li and Matt Harrington. This work is partly supported by grant from National Institute of Health (5R01GM132572(Y. M.), 5R35GM140847(Y.C.), and 1R01GM149659 (L. Y.)). Y.C. is also an investigator of Howard Hughes Medical Institute.

Author contributions

L. Y. conceptualized the study. M.B prepared and purified complex for cryo-EM and performed all structural analysis. X. W. expressed and purified the receptors and different component proteins. X. W. also performed NMR spectral acquisition, data process and spectral analyses in addition to biochemical assessments. J. W. performed the MD simulation. J. X prepared G proteins. W.S prepared part of the receptors and conducted biochemical assays. V.A.A was involved in MD simulation. Y.M. supervised the MD simulation. Y.C supervised the structural analysis. L. Y. supervised receptor and G protein purification, NMR acquisition, and spectral analysis, and biochemical assays. All authors participated in manuscript writing and revisions.

Competing interests

The authors declare no competing financial interests.

697 **Extended Data Figures**

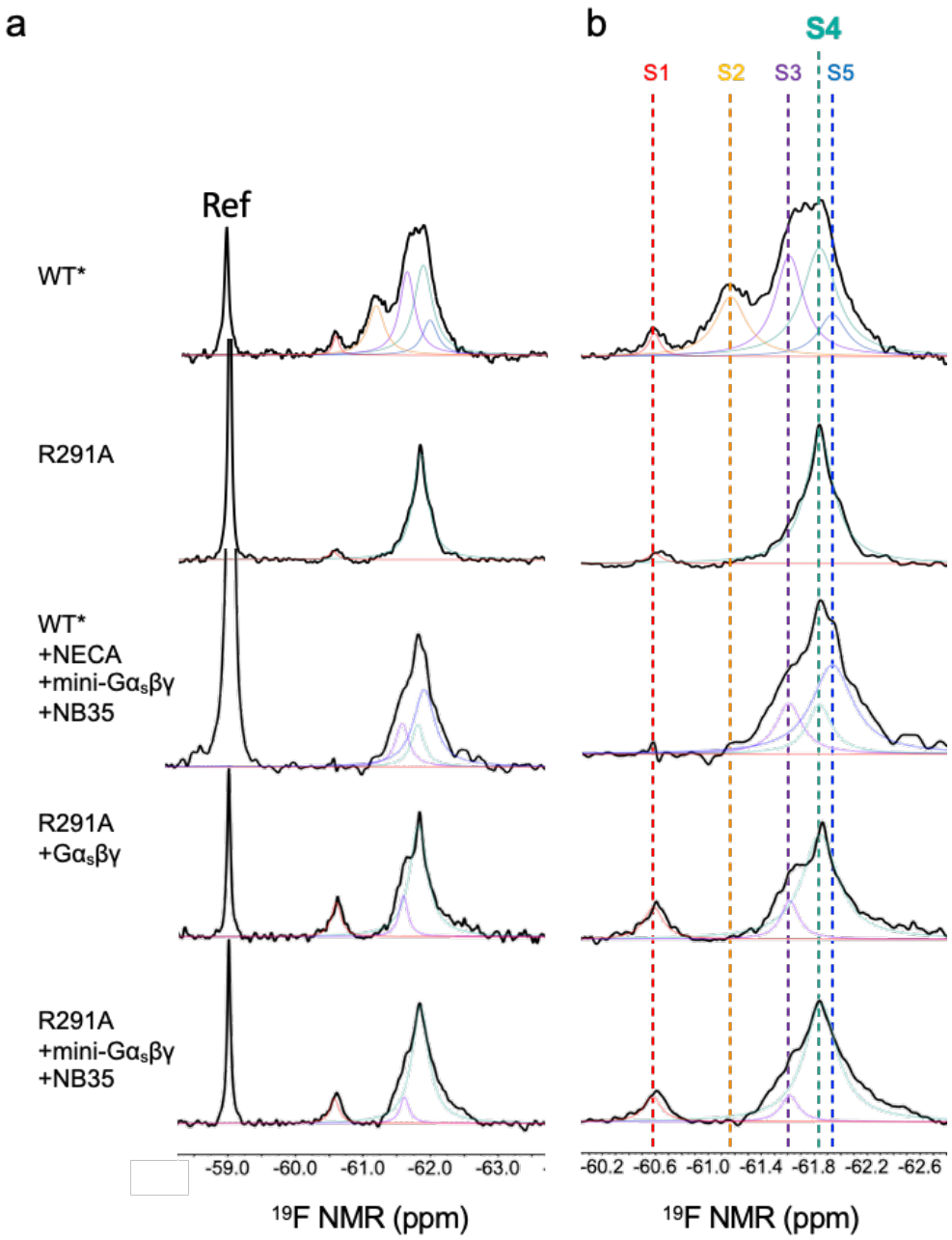

Extended Data Fig. 1: Conformational profiles of the mutant R291A and its complexes probed by ^{19}F-qNMR. (A) and **(B),** Deconvoluted conformational profiles probed by ^{19}F-qNMR as a function of mini-Gαsβγ and Gαsβγ (S4-Gαβγ), in reference to the WT*-mini-Gαsβγ+NB35 (S5-Gαsβγ), representing the conformational profile for the structure PDB ID: 6GDG.

698

699

700

701
702
703
704
705
706
707
708
709

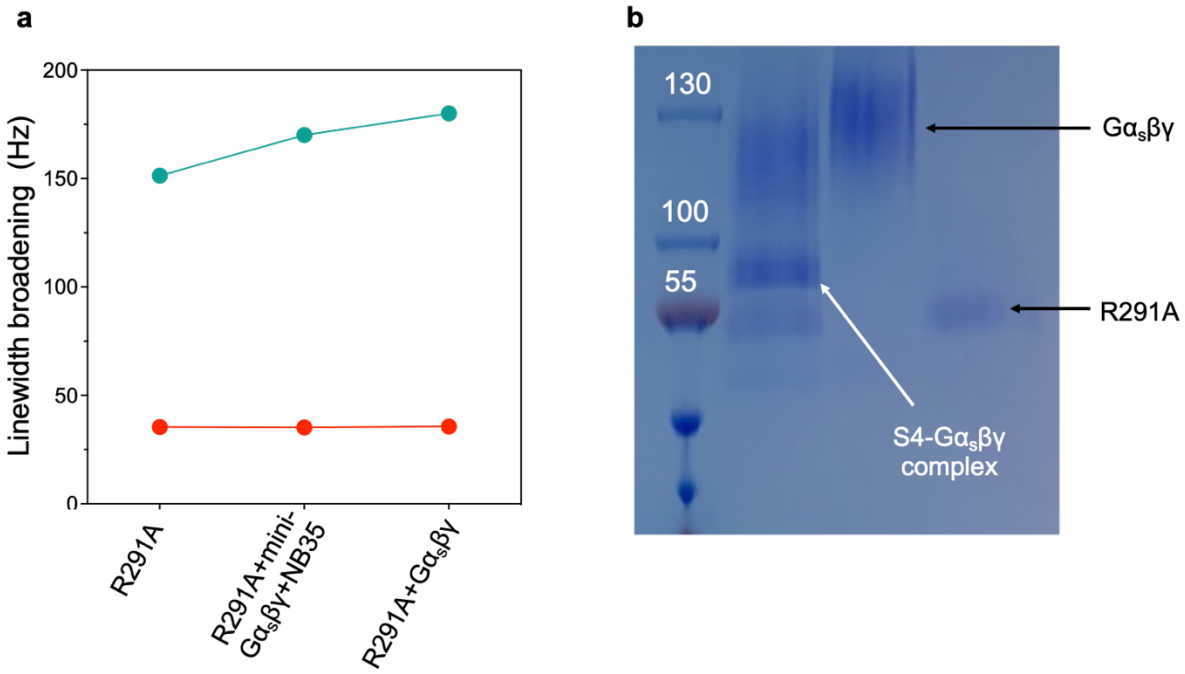

Extended Data Fig. 2: Both linewidth broadening of ^{19}F-qNMR resonance for S4 intermediate and native-PAGE indicated the complex formation between the S4 and G protein. a, Linewidths of S4 resonance for R291A, R291A-G$\alpha_s\beta\gamma$, and R291A-mini-G$\alpha_s\beta\gamma$-NB35. **b,** Native-PAGE for R291A and G$\alpha_s\beta\gamma$ interaction.

710
711
712
713
714
715

716

717

718

719

720

721

722

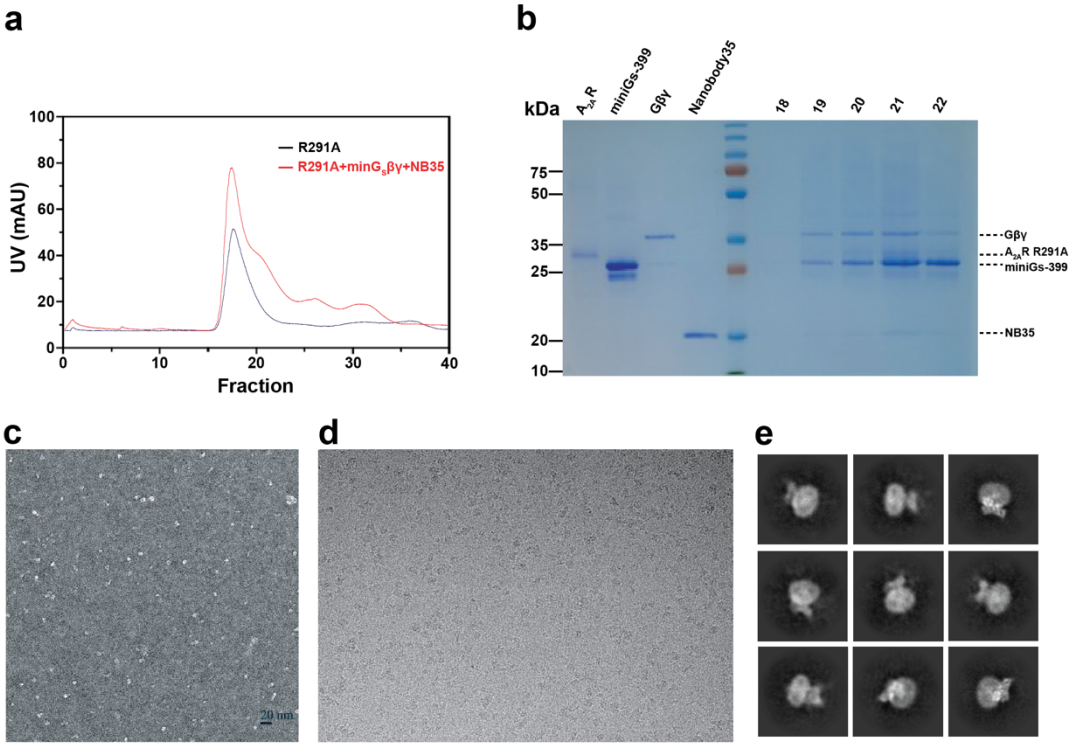

Extended Data Fig. 3: Preparation of $A_{2A}R$ sample and cryo-EM screening. a, Size exclusion chromatography of purified A2AR-R291A with and without mini-$G_s\beta\gamma$+NB35. **b,** SDS-PAGE of the indicated fraction, corresponding to R291A+mini-$G_s\beta\gamma$+NB35. **c**, Negative staining of the R291A+ mini-$G_s\beta\gamma$+NB35 complex. **d**, Representative cryo-EM micrograph of the complex. **e**, Representative 2D average image of the complex.

723

724

725

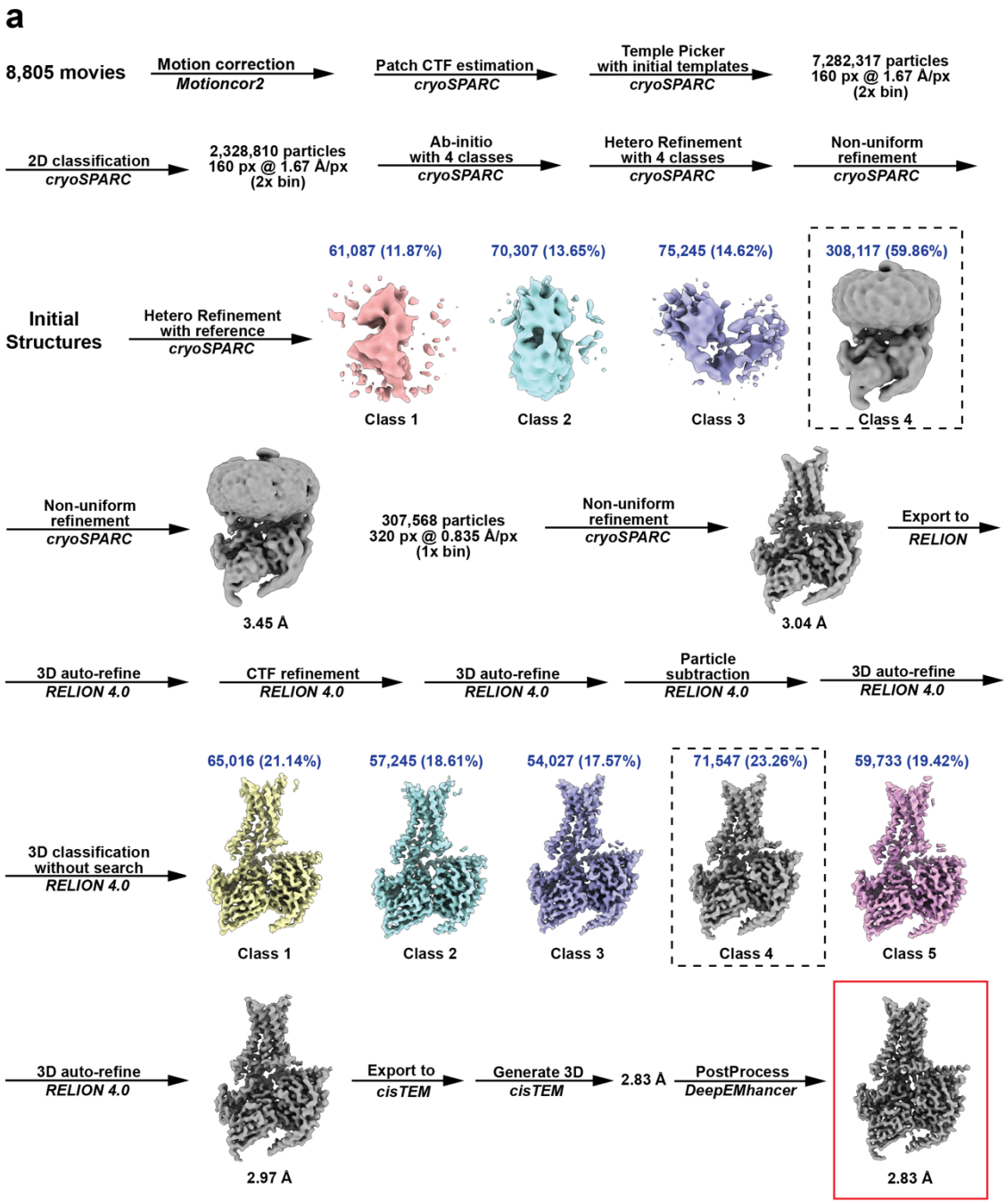

Extended Data Fig. 4: Cryo-EM data and image processing flow. Schematic flow-chat representing the image processing approach for A_{2A}R-R291A. Thumbnail images of each 3D class or refinement are shown along with global GS-FSC resolution in black, particles counts in blue, and dashed black boxes to indicate selected 3D classes. Cryo-EM map (red box) and atomic model are used in main figures to present A_{2A}R-R291A features.

726

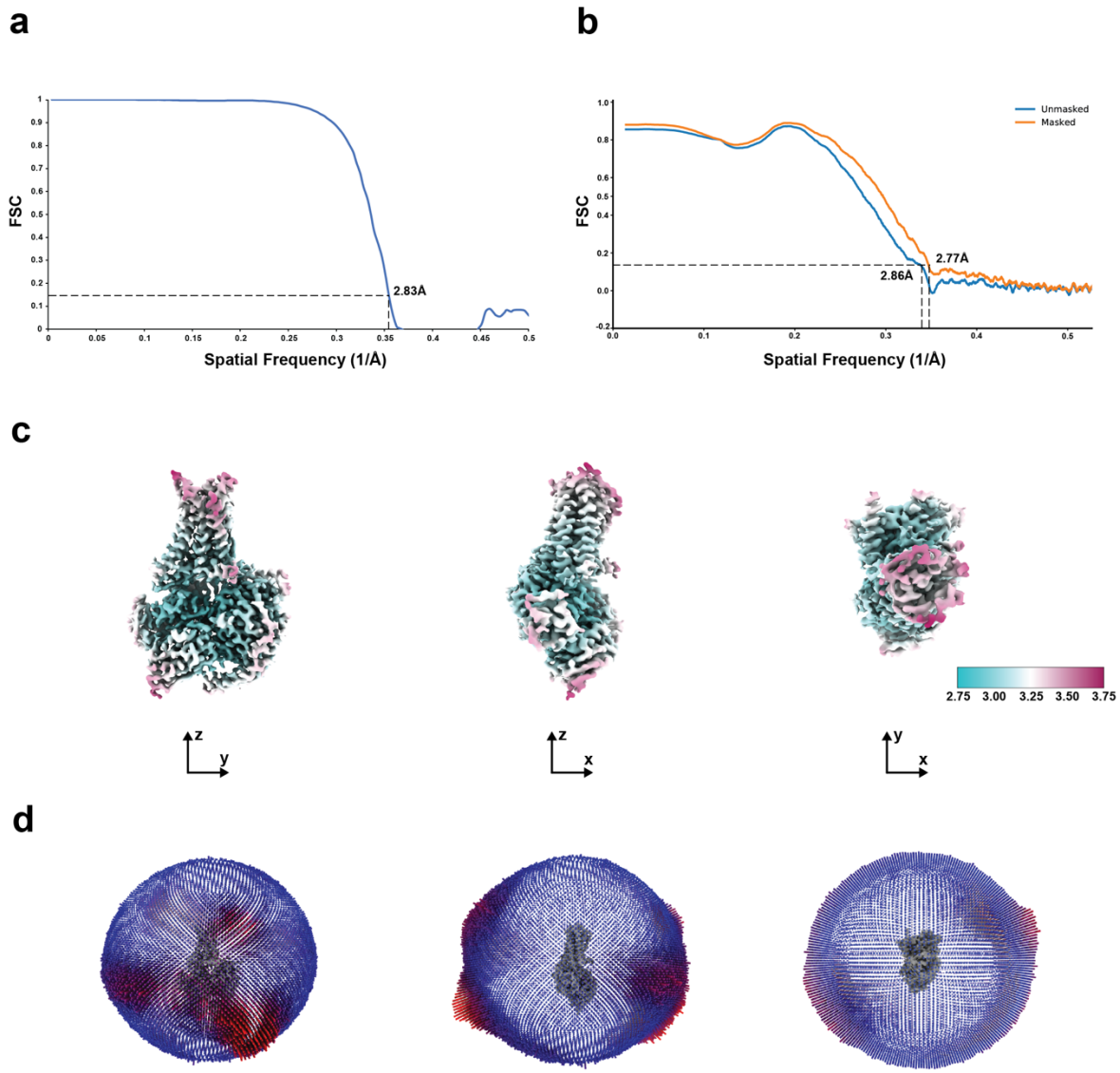

Extended Data Fig. 5: Resolution estimation and atomic model quality. a, Fourier shell correlation curve with resolution determined by the 'gold-standard' FSC. **b,** Model-to-map FSC plots calculated by PHENIX between the map and the model. **c,** Cryo-EM map colored by local resolution estimates using RELION with resolution scale bar (Å). **d**, Histogram representation of the Euler angle distribution from the final particles used in the reconstruction.

733

734

735

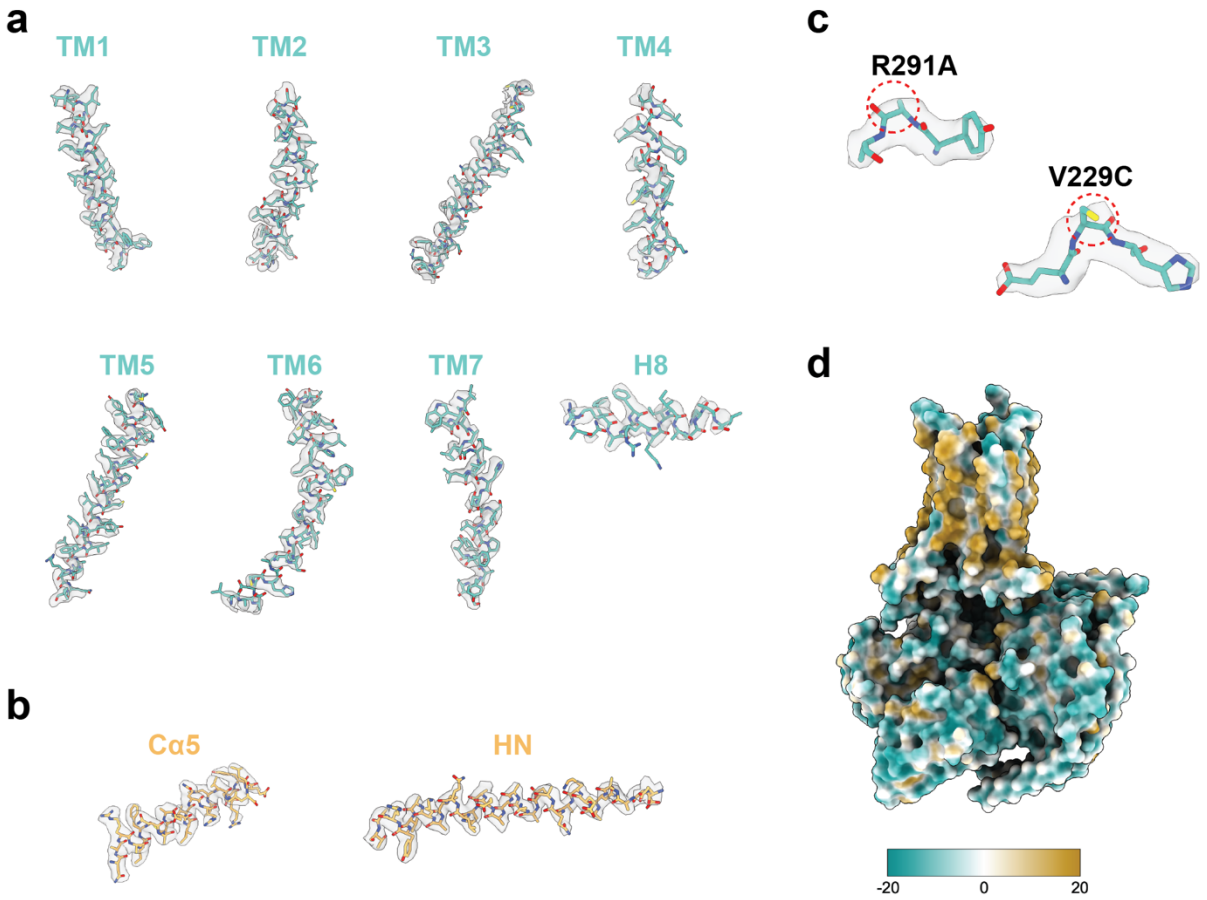

Extended Data Fig. 6: Representative cryo-EM densities from selected structural features of $A_{2A}R$. **a**, Densities of all transmembrane helices. **b**, Representative densities of mini-G. **c,** Cryo-EM densities of V229C and R291A. **d,** Representation of surface hydrophobicity.

736

737

738

739

740

741

742

743

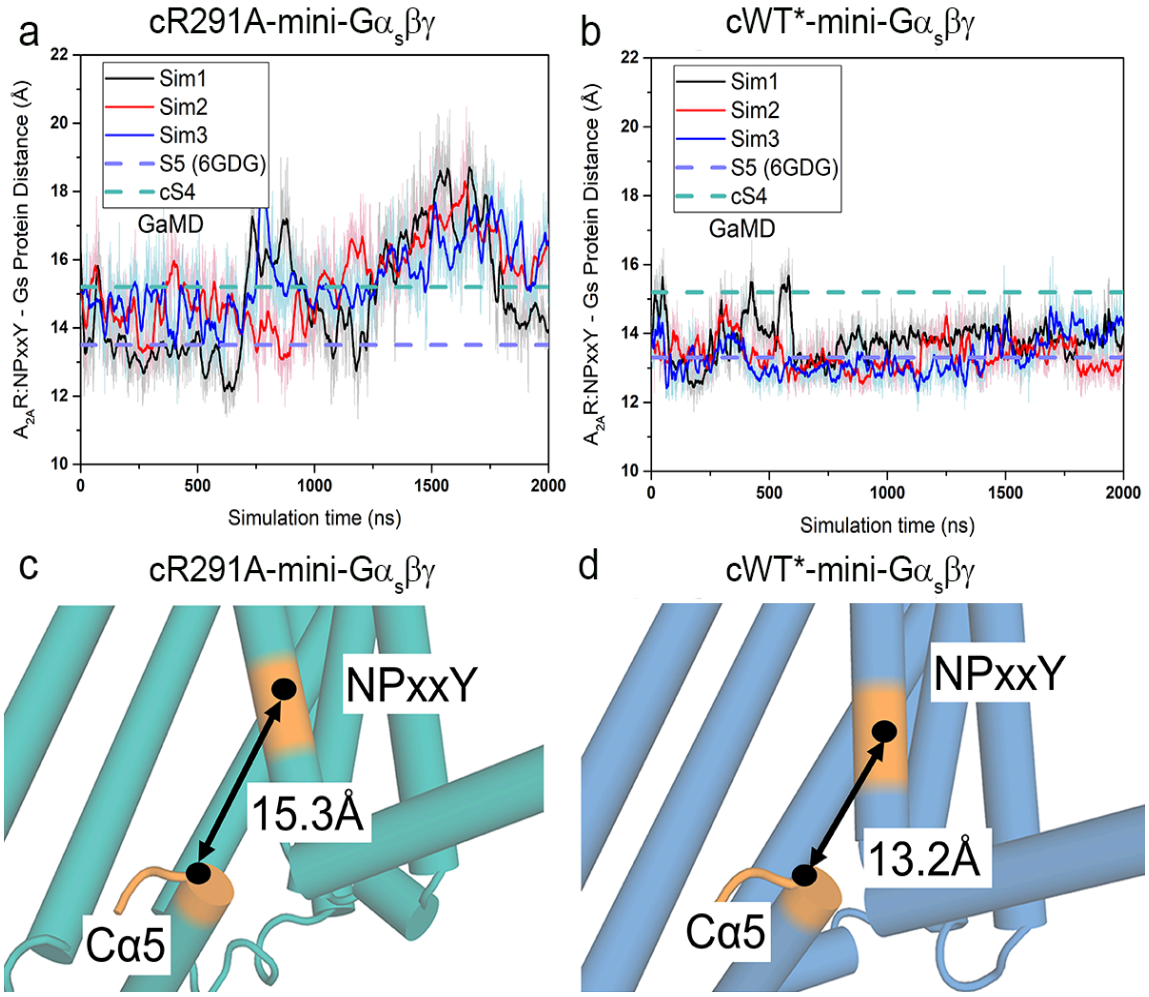

Extended Data Fig. 7: GaMD simulations for cR291A-mini-Gα$_s$βγ and cWT*-mini-Gα$_s$βγ. **a-b**, Time course of the center-of-mass (COM) distance between the receptor NPxxY motif in TM7 and the Cα5 helix (A_{2A}R:NPxxY-Gαs:Cα5 distance) calculated from the GaMD simulations of cR291A-mini-Gα$_s$βγ (**a**) and cWT*-mini-Gα$_s$βγ (**b**) complex systems. **c-d**, Representative low-energy conformations of the cR291A-mini-Gα$_s$βγ (**c**) and **(d)** cWT*-mini-Gα$_s$βγ complex identified from the GaMD simulations. The receptor NPxxY motif and the last five residues of Gα5 helix were colored in orange.

744

745

746

747

748

749

750

751

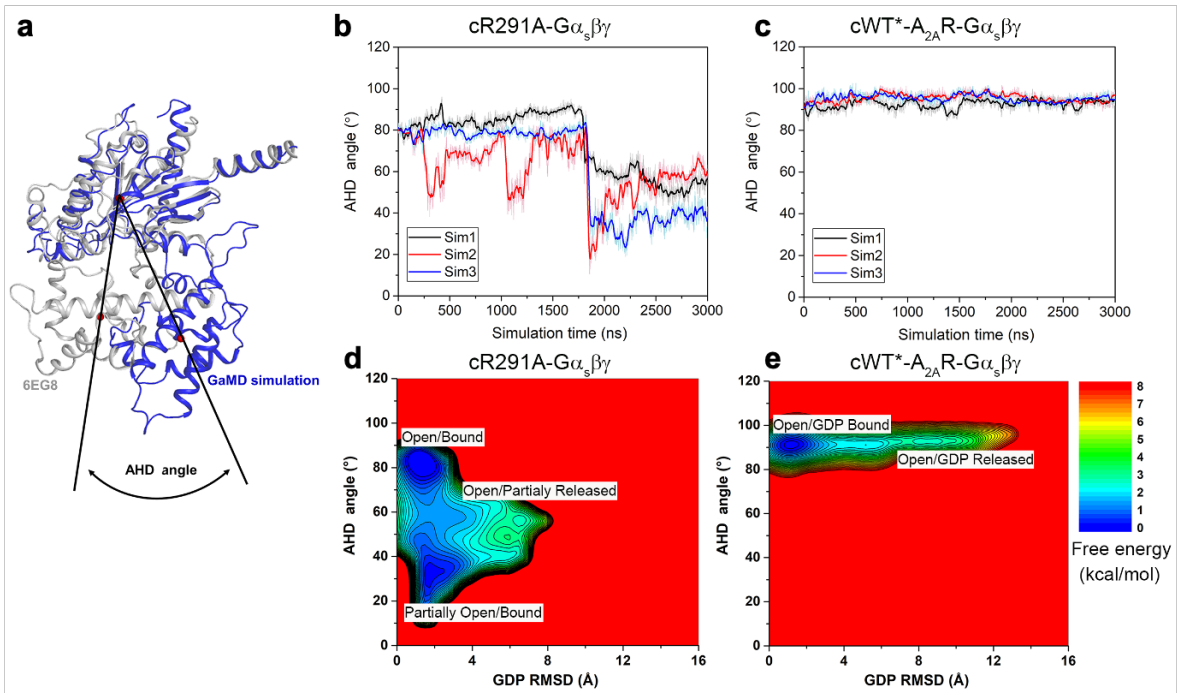

Extended Data Fig. 8: The behaviors of AHD domain in cS4 and cS5 mediated G protein. a, The AHD angle is illustrated by comparing the GaMD simulation conformation with the inactive conformation of $G\alpha_s$ (PDB: 6EG8); Vector 1 goes through centers of the $G\alpha_s$ AHD and Ras-like domain of the inactive conformation (6EG8). Vector 2 goes through the centers of the $G\alpha_s$ AHD and Ras-like domain of the GaMD simulation conformations after aligning the Ras-like domain to the inactive conformation of $G\alpha_s$. **b-c**, The time course of the AHD angle calculated from the GaMD simulations for the *apo* cR291A-$G\alpha_s\beta\gamma$ (**b**) and *apo* cWT*-A_{2A}R-$G\alpha_s\beta\gamma$ (**c**) complexes. **d-e**, 2D free energy profiles of the *apo* cR291A-$G\alpha_s\beta\gamma$ (**d**) and *apo* cWT*-$G\alpha_s\beta\gamma$ (**e**) complexes calculated from GaMD simulations regarding the GDP RMSD and the AHD angle.

752

753

754

755

756

757

758

759

760

761 **References**

762 1 Rasmussen, S. G. *et al.* Crystal structure of the beta2 adrenergic receptor-Gs protein
763 complex. *Nature* **477**, 549-555 (2011). https://doi.org:10.1038/nature10361
764 2 Ye, L., Wang, X., McFarland, A. & Madsen, J. J. (19)F NMR: A promising tool for dynamic
765 conformational studies of G protein-coupled receptors. *Structure* **30**, 1372-1384 (2022).
766 https://doi.org:10.1016/j.str.2022.08.007
767 3 Zhang, Y. *et al.* Cryo-EM structure of the activated GLP-1 receptor in complex with a G
768 protein. *Nature* **546**, 248-253 (2017). https://doi.org:10.1038/nature22394
769 4 Hilger, D. The role of structural dynamics in GPCR-mediated signaling. *FEBS J* **288**, 2461-
770 2489 (2021). https://doi.org:10.1111/febs.15841
771 5 Wang, X., McFarland, A., Madsen, J. J., Aalo, E. & Ye, L. The potential of (19)F NMR
772 application in GPCR biased drug discovery. *Trends Pharmacol Sci* **42**, 19-30 (2021).
773 https://doi.org:10.1016/j.tips.2020.11.001
774 6 Heo, L. & Feig, M. Multi-state modeling of G-protein coupled receptors at experimental
775 accuracy. *Proteins* (2022). https://doi.org:10.1002/prot.26382
776 7 Ye, L., Van Eps, N., Zimmer, M., Ernst, O. P. & Prosser, R. S. Activation of the A_{2A} adenosine
777 G-protein-coupled receptor by conformational selection. *Nature* **533**, 265-268 (2016).
778 https://doi.org:10.1038/nature17668
779 8 Ye, L., Orazietti, A. P., Pandey, A. & Prosser, R. S. High-efficiency expression of yeast-
780 derived G-protein coupled receptors and (19)F labeling for dynamical studies. *Methods*
781 *Mol Biol* **1688**, 407-421 (2018). https://doi.org:10.1007/978-1-4939-7386-6_19
782 9 Perez, D. M. & Karnik, S. S. Multiple signaling states of G-protein-coupled receptors.
783 *Pharmacological reviews* **57**, 147-161 (2005). https://doi.org:10.1124/pr.57.2.2
784 10 Marti-Solano, M., Schmidt, D., Kolb, P. & Selent, J. Drugging specific conformational states
785 of GPCRs: challenges and opportunities for computational chemistry. *Drug discovery*
786 *today* **21**, 625-631 (2016). https://doi.org:10.1016/j.drudis.2016.01.009
787 11 Dong, S. S., Goddard, W. A., 3rd & Abrol, R. Identifying multiple active conformations in
788 the G protein-coupled receptor activation landscape using computational methods.
789 *Methods in cell biology* **142**, 173-186 (2017).
790 https://doi.org:10.1016/bs.mcb.2017.07.009
791 12 Madurga, S., Nedyalkova, M., Mas, F. & Garces, J. L. Ionization and conformational
792 equilibria of citric acid: delocalized proton binding in solution. *The journal of physical*
793 *chemistry. A* **121**, 5894-5906 (2017). https://doi.org:10.1021/acs.jpca.7b05089
794 13 Wang, X., Neale, C., Kim, S. K., Goddard, W. A. & Ye, L. Intermediate-state-trapped
795 mutants pinpoint G protein-coupled receptor conformational allostery. *Nat Commun* **14**,
796 1325 (2023). https://doi.org:10.1038/s41467-023-36971-6
797 14 Dore, A. S. *et al.* Structure of the adenosine A2A receptor in complex with ZM241385 and
798 the xanthines XAC and caffeine. *Structure* **19**, 1283-1293 (2011).
799 https://doi.org:10.1016/j.str.2011.06.014
800 15 Jaakola, V. P. *et al.* The 2.6 angstrom crystal structure of a human A2A adenosine receptor
801 bound to an antagonist. *Science* **322**, 1211-1217 (2008).
802 https://doi.org:10.1126/science.1164772

803 16 Garcia-Nafria, J., Lee, Y., Bai, X., Carpenter, B. & Tate, C. G. Cryo-EM structure of the
804 adenosine A(2A) receptor coupled to an engineered heterotrimeric G protein. *Elife* **7**
805 (2018). https://doi.org:10.7554/eLife.35946
806 17 Kenakin, T. New concepts in pharmacological efficacy at 7TM receptors: IUPHAR review
807 2. *Br J Pharmacol* **168**, 554-575 (2013). https://doi.org:10.1111/j.1476-
808 5381.2012.02223.x
809 18 Mahoney, J. P. & Sunahara, R. K. Mechanistic insights into GPCR-G protein interactions.
810 *Curr Opin Struct Biol* **41**, 247-254 (2016). https://doi.org:10.1016/j.sbi.2016.11.005
811 19 Huang, S. K. *et al.* Allosteric modulation of the adenosine A(2A) receptor by cholesterol.
812 *Elife* **11** (2022). https://doi.org:10.7554/eLife.73901
813 20 Huang, S. K. *et al.* Delineating the conformational landscape of the adenosine A(2A)
814 receptor during G protein coupling. *Cell* **184**, 1884-1894 e1814 (2021).
815 https://doi.org:10.1016/j.cell.2021.02.041
816 21 Du, Y. *et al.* Assembly of a GPCR-G protein complex. *Cell* **177**, 1232-1242 e1211 (2019).
817 https://doi.org:10.1016/j.cell.2019.04.022
818 22 Bai, C. *et al.* Exploring the Activation Process of the beta2AR-Gs Complex. *J Am Chem Soc*
819 **143**, 11044-11051 (2021). https://doi.org:10.1021/jacs.1c03696
820 23 Wacker, D. *et al.* Structural features for functional selectivity at serotonin receptors.
821 *Science* **340**, 615-619 (2013). https://doi.org:10.1126/science.1232808
822 24 Zondlo, N. J. Aromatic-proline interactions: electronically tunable CH/pi interactions. *Acc*
823 *Chem Res* **46**, 1039-1049 (2013). https://doi.org:10.1021/ar300087y
824 25 Shi, L. *et al.* Beta2 adrenergic receptor activation. Modulation of the proline kink in
825 transmembrane 6 by a rotamer toggle switch. *J Biol Chem* **277**, 40989-40996 (2002).
826 https://doi.org:10.1074/jbc.M206801200
827 26 Ragnarsson, L., Andersson, A., Thomas, W. G. & Lewis, R. J. Mutations in the NPxxY motif
828 stabilize pharmacologically distinct conformational states of the alpha(1B)- and beta(2)-
829 adrenoceptors. *Sci Signal* **12** (2019). https://doi.org:10.1126/scisignal.aas9485
830 27 Cherezov, V. *et al.* High-resolution crystal structure of an engineered human beta2-
831 adrenergic G protein-coupled receptor. *Science* **318**, 1258-1265 (2007).
832 https://doi.org:10.1126/science.1150577
833 28 Westfield, G. H. *et al.* Structural flexibility of the G alpha s alpha-helical domain in the
834 beta2-adrenoceptor Gs complex. *Proc Natl Acad Sci U S A* **108**, 16086-16091 (2011).
835 https://doi.org:10.1073/pnas.1113645108
836 29 Duan, J. *et al.* Structures of full-length glycoprotein hormone receptor signalling
837 complexes. *Nature* **598**, 688-692 (2021). https://doi.org:10.1038/s41586-021-03924-2
838 30 J., G. A. An introduction of Hydrogen bonding. *Oxford Unviersity Press* (1998).
839 31 Papasergi-Scott, M. M. *et al.* Time-resolved cryo-EM of G-protein activation by a GPCR.
840 *Nature* (2024). https://doi.org:10.1038/s41586-024-07153-1
841 32 Flock, T. *et al.* Universal allosteric mechanism for Galpha activation by GPCRs. *Nature* **524**,
842 173-179 (2015). https://doi.org:10.1038/nature14663
843 33 Papasergi-Scott, M. M. *et al.* Time-resolved cryo-EM of G protein activation by a GPCR.
844 *bioRxiv* (2023). https://doi.org:10.1101/2023.03.20.533387

34 Dror, R. O. *et al.* SIGNAL TRANSDUCTION. Structural basis for nucleotide exchange in heterotrimeric G proteins. *Science* **348**, 1361-1365 (2015). https://doi.org:10.1126/science.aaa5264

35 Zhao, W., Wang, X. & Ye, L. Expression and purification of yeast-derived GPCR, Gα and Gβγ subunits for structural and dynamic studies. *Bio Protoc* **11**, e3919 (2021). https://doi.org:10.21769/BioProtoc.3919

36 Carpenter, B. & Tate, C. G. Engineering a minimal G protein to facilitate crystallisation of G protein-coupled receptors in their active conformation. *Protein Eng Des Sel* **29**, 583-594 (2016). https://doi.org:10.1093/protein/gzw049

37 Carpenter, B. & Tate, C. G. Expression and purification of mini G proteins from Escherichia coli. *Bio-protocol* **7**, e2235-e2235 (2017).

38 Mondal, S., Hsiao, K. & Goueli, S. A. A homogenous bioluminescent system for measuring GTPase, GTPase activating protein, and guanine nucleotide exchange factor activities. *Assay Drug Dev Technol* **13**, 444-455 (2015). https://doi.org:10.1089/adt.2015.643

39 Wang, J. N. *et al.* Gaussian accelerated molecular dynamics: Principles and applications. *Wires Comput Mol Sci* **11**, e1521 (2021). https://doi.org:10.1002/wcms.1521

40 Miao, Y., Feher, V. A. & McCammon, J. A. Gaussian Accelerated Molecular Dynamics: Unconstrained Enhanced Sampling and Free Energy Calculation. *Journal of Chemical Theory and Computation* **11**, 3584-3595 (2015). https://doi.org:10.1021/acs.jctc.5b00436

41 Waterhouse, A. *et al.* SWISS-MODEL: homology modelling of protein structures and complexes. *Nucleic Acids Res* **46**, W296-W303 (2018). https://doi.org:10.1093/nar/gky427

42 Hu, Q. & Shokat, K. M. Disease-Causing Mutations in the G Protein Gαs Subvert the Roles of GDP and GTP. *Cell* **173**, 1254-1264.e1211 (2018). https://doi.org:10.1016/j.cell.2018.03.018

43 Vanommeslaeghe, K. & MacKerell, A. D. CHARMM additive and polarizable force fields for biophysics and computer-aided drug design. *Biochimica et Biophysica Acta (BBA) - General Subjects* **1850**, 861-871 (2015). https://doi.org:10.1016/j.bbagen.2014.08.004

44 Huang, J. *et al.* CHARMM36m: an improved force field for folded and intrinsically disordered proteins. *Nature Methods* **14**, 71 (2016). https://doi.org:10.1038/nmeth.4067

45 Klauda, J. B. *et al.* Update of the CHARMM All-Atom Additive Force Field for Lipids: Validation on Six Lipid Types. *The Journal of Physical Chemistry B* **114**, 7830-7843 (2010). https://doi.org:10.1021/jp101759q

46 Vanommeslaeghe, K. & MacKerell, A. D. Automation of the CHARMM general force field (CGenFF) I: Bond perception and atom typing. *Journal of Chemical Information and Modeling* **52**, 3144-3154 (2012). https://doi.org:10.1021/ci300363c

47 Darden, T., York, D. & Pedersen, L. Particle mesh Ewald: An N· log (N) method for Ewald sums in large systems. *J Chem Physics* **98**, 10089 (1993).

48 D.A. Case, D.S. Cerutti, T.E. Cheatham, III, T.A. Darden, R.E. Duke, T.J. Giese, H. Gohlke, A.W. Goetz, D. Greene, N. Homeyer, S. Izadi, A. Kovalenko, T.S. Lee, S. LeGrand, P. Li, C. Lin, J. Liu, T. Luchko, R. Luo, D. Mermelstein, K.M. Merz, G. Monard, H. Nguyen, I. Omelyan, A. Onufriev, F. Pan, R. Qi, D.R. Roe, A. Roitberg, C. Sagui, C.L. Simmerling, W.M. Botello-Smith, J. Swails, R.C. Walker, J. Wang, J. Wang, R.M. Wolf, X. Wu, L. Xiao, D.M. York and P.A. Kollman (2022), AMBER 2022, University of California, San Francisco.

49 Miao, Y., Feher, V. A. & McCammon, J. A. Gaussian Accelerated Molecular Dynamics: Unconstrained Enhanced Sampling and Free Energy Calculation. *J Chem Theor Comput* **11**, 3584-3595 (2015). https://doi.org:10.1021/acs.jctc.5b00436

50 Wang, J. *et al.* Gaussian accelerated molecular dynamics (GaMD): principles and applications. *Wiley Interdiscip Rev Comput Mol Sci* **11**, e1521 (2021). https://doi.org:10.1002/wcms.1521

51 Roe, D. R. & Cheatham, T. E., 3rd. PTRAJ and CPPTRAJ: software for processing and analysis of molecular dynamics trajectory data. *J. Chem. Theory Comput.* **9**, 3084-3095 (2013). https://doi.org:10.1021/ct400341p

52 Miao, Y. *et al.* Improved reweighting of accelerated molecular dynamics simulations for free energy calculation. *J. Chem. Theory Comput.* **10**, 2677-2689 (2014). https://doi.org:10.1021/ct500090q

53 Ohi, M., Li, Y., Cheng, Y. & Walz, T. Negative staining and image classification - powerful tools in modern electron microscopy. *Biol Proced Online* **6**, 23-34 (2004). https://doi.org:10.1251/bpo70

54 Mastronarde, D. N. Automated electron microscope tomography using robust prediction of specimen movements. *J Struct Biol* **152**, 36-51 (2005). https://doi.org:10.1016/j.jsb.2005.07.007

55 Zheng, S. Q. *et al.* MotionCor2: anisotropic correction of beam-induced motion for improved cryo-electron microscopy. *Nat Methods* **14**, 331-332 (2017). https://doi.org:10.1038/nmeth.4193

56 Punjani, A., Rubinstein, J. L., Fleet, D. J. & Brubaker, M. A. cryoSPARC: algorithms for rapid unsupervised cryo-EM structure determination. *Nat Methods* **14**, 290-296 (2017). https://doi.org:10.1038/nmeth.4169

57 Scheres, S. H. RELION: implementation of a Bayesian approach to cryo-EM structure determination. *J Struct Biol* **180**, 519-530 (2012). https://doi.org:10.1016/j.jsb.2012.09.006

58 Pettersen, E. F. *et al.* UCSF Chimera--a visualization system for exploratory research and analysis. *J Comput Chem* **25**, 1605-1612 (2004). https://doi.org:10.1002/jcc.20084

59 Grant, T., Rohou, A. & Grigorieff, N. cisTEM, user-friendly software for single-particle image processing. *Elife* **7** (2018). https://doi.org:10.7554/eLife.35383

60 Rosenthal, P. B. & Henderson, R. Optimal determination of particle orientation, absolute hand, and contrast loss in single-particle electron cryomicroscopy. *J Mol Biol* **333**, 721-745 (2003). https://doi.org:10.1016/j.jmb.2003.07.013

61 Sanchez-Garcia, R. *et al.* DeepEMhancer: a deep learning solution for cryo-EM volume post-processing. *Commun Biol* **4**, 874 (2021). https://doi.org:10.1038/s42003-021-02399-1

62 Goddard, T. D. *et al.* UCSF ChimeraX: Meeting modern challenges in visualization and analysis. *Protein Sci* **27**, 14-25 (2018). https://doi.org:10.1002/pro.3235

63 Croll, T. I. ISOLDE: a physically realistic environment for model building into low-resolution electron-density maps. *Acta Crystallogr D Struct Biol* **74**, 519-530 (2018). https://doi.org:10.1107/S2059798318002425

931 64 Emsley, P. & Cowtan, K. Coot: model-building tools for molecular graphics. *Acta*
932 *Crystallogr D Biol Crystallogr* **60**, 2126-2132 (2004).
933 https://doi.org:10.1107/S0907444904019158
934 65 Afonine, P. V. *et al.* Towards automated crystallographic structure refinement with
935 phenix.refine. *Acta Crystallogr D Biol Crystallogr* **68**, 352-367 (2012).
936 https://doi.org:10.1107/S0907444912001308
937 66 Berman, H., Henrick, K. & Nakamura, H. Announcing the worldwide Protein Data Bank.
938 *Nat Struct Biol* **10**, 980 (2003). https://doi.org:10.1038/nsb1203-980
939